

THE DEVELOPMENT OF AN ACCELERATED TESTING FACILITY FOR THE
STUDY OF DEPOSITS IN LAND-BASED GAS TURBINE ENGINES

by

Jared W. Jensen

A thesis submitted to the faculty of

Brigham Young University

In partial fulfillment of the requirements for the degree of

Master of Science

Department of Mechanical Engineering

Brigham Young University

August 2004

Copyright © 2004 Jared W. Jensen

All Rights Reserved

BRIGHAM YOUNG UNIVERSITY

GRADUATE COMMITTEE APPROVAL

of a thesis submitted by

Jared W. Jensen

This thesis has been read by each member of the following graduate committee and by majority vote has been found to be satisfactory.

Date

Jeffrey P. Bons, Chair

Date

Thomas H. Fletcher

Date

Brent W. Webb

BRIGHAM YOUNG UNIVERSITY

As chair of the candidate's graduate committee, I have read the thesis of Jared W. Jensen in its final form and have found that (1) its format, citations, and bibliographical style are consistent and acceptable and fulfill university and department style requirements; (2) its illustrative materials including figures, tables, and charts are in place; and (3) the final manuscript is satisfactory to the graduate committee and is ready for submission to the university library.

Date

Jeffrey P. Bons
Chair, Graduate Committee

Accepted for the Department

Brent L. Adams
Graduate Coordinator

Accepted for the College

Douglas M. Chabries
Dean, Ira A. Fulton College of Engineering
and Technology

ABSTRACT

THE DEVELOPMENT OF AN ACCELERATED TESTING FACILITY FOR THE STUDY OF DEPOSITS IN LAND-BASED GAS TURBINE ENGINES

Jared W. Jensen

Department of Mechanical Engineering

Master of Science

Turbine engine efficiency modeling depends on many parameters related to fluid dynamics and heat transfer. Many of these parameters change dynamically once the engine enters service and begins to experience surface degradation. This thesis presents a validation of the design and operation of an accelerated testing facility for the study of foreign deposit layers typical to the operation of land-based gas turbines. It also reports on the use of this facility in an effort to characterize the change in thermal resistance on the surface of turbine blades as deposits accumulate. The facility was designed to produce turbine deposits in a 4-hour test that would simulate 10,000 hours of turbine operation. This is accomplished by matching the net foreign particulate throughput of an actual gas turbine. Flow Mach number, temperature and particulate impingement angle are also matched. Validation tests were conducted to model the ingestion of foreign particulate typically found in the urban environment. The majority of this particulate is

ceramic in nature and smaller than 10 microns in size, but varies in size up to 80 microns. Deposits were formed for flow Mach number and temperature of 0.3 and 1150°C respectively, using air plasma sprayed (APS) thermal barrier coat (TBC) material coupons donated from industry. These conditions are typical of a modern, first stage nozzle. Investigations over a range of impingement angles yielded samples with deposit thicknesses from 50 to 200 microns in 4-hour, accelerated-service simulations. Above a threshold temperature, deposit thickness was dependent primarily upon particle concentration. Test validation was achieved using direct comparison with deposits from service hardware. Deposit characteristics affecting blade heat transfer via convection and conduction were assessed. Surface topography analysis indicated that the surface structure of the generated deposits were similar to those found on actual turbine blades. Scanning electron microscope (SEM) and x-ray spectroscopy analyses indicated that the deposit microstructures and chemical compositions were comparable to turbine blade deposit samples obtained from industry. A roadmap for the development of a theoretical model of thermal resistance using the SEM scan is presented. Thermal resistance experiments conducted with deposit samples indicate that a general decrease in thermal resistance occurs as the samples are exposed to operating conditions in the accelerated testing facility. This is likely due to sintering effects within the TBC dominating any thermal resistance increase arising from deposition. Recommendations for future research into the interaction between TBC sintering and deposit evolution are presented.

ACKNOWLEDGEMENTS

This work could not have been completed without the great support provided by many students, staff, and faculty of Brigham Young University and particularly the mechanical engineering department. Special thanks are given to the talented machinists of the Precision Machine Lab and Mechanical Engineering machine shop who were instrumental in bringing my equipment designs into reality, James Wammack and John Pettitt whose assistance was crucial in building and operating the accelerated test facilities used for this research, Sean Squire for his endless patience with the SEM, and Dr. Thomas Fletcher for providing his expertise, access to specialized equipment, and encouragement throughout the long hard slog. Most especially, Dr. Jeffrey Bons deserves great thanks for pushing me to expect more of myself, to achieve, and perform at the highest level possible. Though I could not always give my thanks through the many months of work, I give it now without reservation.

TABLE OF CONTENTS

TABLE OF CONTENTS.....	viii
Chapter 1: Introduction.....	1
Gas Turbine Engines.....	4
Deposition.....	5
Present State of the Art.....	6
Motivations and Theoretical Foundations.....	9
Procedures for Experimentation.....	15
Summary.....	17
Chapter 2: An Accelerated Testing Facility.....	19
The Combustor.....	21
Particulate.....	24
Instrumentation.....	30
Chapter 3: Validation of the Structure of Deposits Formed in Accelerated Testing.....	33
Topography.....	34
Internal Structure & Chemical Composition.....	40
Influence of Angle.....	47
Influence of Particulate Concentration.....	49
Influence of Temperature.....	50
Chapter 4: A Proposed Method for a Theoretical Estimate of the Thermal Resistance of Deposit Layers.....	51
Chapter 5: Experimental Determination of Thermal Resistance in 1-D Heat Flow.....	67
The Experimental Specimens.....	68
Experimental Apparatus.....	69
Chapter 6: Thermal Resistance Measurement and Analysis.....	77
Thermal Resistance Analysis.....	79
Sintering and Deposition.....	80
Chapter 7: Conclusions and Recommendations.....	83
Conclusions.....	83
Lessons Learned.....	84
Recommendations.....	85
Future Research.....	86
Appendix A: Bibliography.....	89
Appendix B: Nomenclature.....	93
Appendix C: Operational Procedures for Accelerated Testing Facility.....	96
Exhaust System.....	96
Fuel System.....	96
Operation Procedures.....	98

Appendix D: CR-ROM Content Guide.....	102
SEM Pictures	102
Matlab Code.....	103
Appendix E: Sample Code for Theoretical Analysis of Deposit SEM Images	104
Module I: Gradient Definitions.....	105
Module IV: Tortuosity	107

Chapter 1: Introduction

Despite the greatest of precautions and most stringent filtering techniques, it is nearly impossible to economically provide completely clean air streams in gas turbine (GT) engines. Sand, pollutants, and moisture may all be introduced into the flow and degrade exposed surfaces in the engine. Internal sources of particulate such as dirty fuels, eroded components, and secondary chemical reactions also contribute to the flow of solid and semi-molten matter passing through the GT engine. These particles may either pass through the engine with no effect or attack the surfaces of the engine through erosion, corrosion, or deposition. The adverse effects of these three degradation mechanisms are well documented in the literature.

Erosion can cause significant reductions in engine performance by opening up tip clearances and altering blade contours. For example, Ghenaiet et al. reported a 6-10% loss in adiabatic efficiency for 6 hours of sand ingestion in an axial fan (Ghenaiet et al, 2001). Deposition poses the opposite problem by clogging critical bleed pathways and reducing blade flow passages. Wenglarz proposed a model for estimating the critical loss in turbine power that occurs when the choked mass flow limit is reduced due to deposit buildup at the nozzle guide vane passage throat (Wenglarz, 1992). Kim et al.

documented the disastrous results of film cooling holes being plugged by massive ingestion from simulated volcanic ash (Kim et al, 1993). Both erosion and deposition are also known to increase levels of surface roughness which produces corresponding increases in heat transfer (up to 50%) and skin friction (up to 300%) (Bons, 2002). Finally, all three degradation mechanisms (including corrosion) reduce part life and increase the risk of an unexpected run-time failure.

For the case of deposition in particular, a better understanding of the characteristics of the materials deposited on turbine surfaces would allow a more accurate estimate of their impact on the efficiency and survivability of turbine blades. As GT engine technology has evolved from F-class to G-class and now to H-class, the increase in turbine inlet temperature (TIT) from 1300°C to 1500°C has increased thermal efficiency from 55% to near 60% for H-class turbines (Suao, 2000). As the US Department of Energy (DOE) contemplates the large-scale introduction of dirty fuels such as coal and biomass in H-type, high temperature turbine engines, the need to understand deposition mechanisms and their effects on efficiency at high temperatures will increase dramatically.

The capability of research facilities to study turbine deposition characteristics for high temperature service is presently limited by the time required to develop realistic deposits in typical operating engines. Depending on the operation schedule and environment of a land-based GT, the formation of deposits may require as much as 25,000 hours of operation. To reproduce this in a laboratory study would require months or years of preparation time for a single sample. This limitation obviates the need to explore the

possibility of accelerated testing procedures. Without an accelerated testing method, any comprehensive investigation of new service conditions that may affect the characteristics of deposit growth would clearly be impractical.

This work investigates the suitability of such an accelerated deposition facility to specifically study the deposition of ingested particulate on the first stage turbine blades in land based GT engines. An accelerated testing facility has been developed to produce realistic deposits on turbine blade materials. Sample turbine blade materials with thermal barrier coatings (TBCs) representative of common GT engine construction have been obtained from various gas turbine manufacturers including General Electric, Siemens-Westinghouse, and Solar Turbines. Because of non-disclosure agreements with each of these companies, no specification shall be made forthwith regarding the providence of particular samples discussed later in this work. Deposits have been generated on these materials in a new accelerated testing facility. At the same time, actual turbine blades at various points in their service life have been obtained from the gas turbine community. These serviced components have been characterized to determine the structure of surface deposits including an examination of surface roughness, morphology, internal structure including porosity, and chemical composition. A comparison of these findings to the results of similar examinations of accelerated deposits that have been reported in the literature is used to validate this testing procedure before proceeding to a further analysis of the thermophysical properties of the deposit layer.

Gas Turbine Engines

Gas turbine (GT) engines in power plants across the world provide much of the power used in commercial electrical grids. Depending on the operating environment, fuel quality, maintenance considerations, loading, and many other parameters, turnover maintenance intervals on GT engines can range in length from 6 months to 5 years or more. Many of these parameters are greatly affected by the development of deposits from foreign materials, making a study of foreign material deposition modes critical to a comprehensive understanding of GT service life.

Turbine blade life is so sensitive to metal surface temperature that a 50°C error in predicting that temperature may result in a 50% difference in predicted effective life (Rivir, 2002). Much research has been done to characterize the degradation in performance of turbine blades due to extreme service conditions, exposure to adverse environmental effects, erosion, surface spalling, and various other abuses. However, though several researchers have studied various degradation modes, their thermal evaluation of the decrement in performance has been based on a “clean” turbine blade that accounts for increased convective heat transfer due to increased roughness, but not the physical presence of deposit layers. Dr. Fred Soechting, a former researcher with Pratt & Whitney stated that “the design assumptions are that this [deposit] layer does not exist and the thermal boundary conditions are placed on the external [blade] surface” (Soechting, 2003). The author is unaware of any research upon the effect of deposits or residue altering the ability of turbine blades to cope with thermal stress and high temperature, particularly as part of the heat conduction system. Because any material with a finite thermal conductivity has the ability to thermally insulate a substrate, this

work has studied the possibility that the deposits on turbine blades may actually increase the survivability of the blade beyond present predictions that do not account for insulation protection provided by the deposit.

Deposition

Despite the greatest of precautions and most stringent filtering techniques, it is impossible (or at the very least, highly uneconomical) to use entirely clean air streams in the combustion process. Sand, pollutants, and moisture may all be introduced into the gas turbine engine during the combustion process. These particulates will erode other parts of the engine—thereby increasing the total volume of particulate and greatly increasing its diversity by introducing the exotic materials of turbine construction into the particulate mix—and then either pass completely through the engine or deposit themselves on the engine's internal surfaces.

The development of foreign deposits on the turbine blades in the GT engine form one of the primary considerations in the development of a cyclic maintenance plan. As deposits form, they present many problems for continued optimal performance. Deposits greatly increase the surface roughness of GT engine components. This causes an increase in convective heat transfer by as much as 40% (Bons et al., 2001). Foreign deposits can grow large enough to alter the bulk gas flow paths by changing the physical geometry of the blades on a macroscopic scale. Deposition also provides a reaction site that catalyzes corrosion and other forms of chemical attack. This can undermine the protective benefits of coatings and other material considerations designed to protect the blade from high temperature failures. Deposit growth can also greatly affect the overall heat transfer

through blades by clogging cooling holes used for film cooling. Reducing the flow of cooling air through the blade can also have the effect of augmenting other temperature-dependant failure modes such as thermal stress cracking, creep, and corrosion by elevating the temperature of the turbine blade without any other change in operating conditions.

By understanding the effect that deposits have on these various mechanisms, manufacturers hope to balance the maintenance requirements of large GT engines against the financial demands of operating multi-million dollar power generation facilities. Maintenance schedules are taxed to the limit to ensure that maximum service time is achieved at minimal maintenance expense without undue risk of catastrophic failure or unplanned shutdown—both of which can easily cost much more than an extra service cycle. By increasing the understanding of the deposition phenomenon, the service envelope can be pushed more aggressively and more safely, resulting in a potentially substantial monetary savings to the GT industry.

Present State of the Art

Particulate flow in GT engines (either from ingestion, dirty fuel combustion, internal erosion, or a combination of factors) results in three adverse phenomena: corrosion, erosion, and deposition. Corrosion in the HP turbine is primarily due to attack of the surface, particularly the coating, by hot gases and particles. A model has been presented by Chan et al. to characterize the life of coatings when considering oxidation, fracture and spallation in the coating, inward diffusion of Al from the coating to the substrate, and the critical level of Al compounds (typically Al_2O_3) required at the surface to form a

protective oxide layer (Chan et al, 1999). Critical temperature thresholds for Type I and Type II (Hot Corrosion) are 850-1000°C and 700°C respectively (Krishnan et al, 2003). While these temperature regimes are well below the inlet gas temperature for most modern turbines, they become relevant in regions of film cooling (where the metal temperature is lower than gas temperature) and in subsequent turbine stages. Deposition rate can have an effect on the rate of hot corrosion by influencing the rate of mass flux of sulfur to the wall (Krishnan et al, 2003). Thus, an understanding of depositional mechanisms and particularly their interaction with sulfur compounds would aid in the understanding of Type I and II corrosion attacks in GT engines. An equally destructive deposition mechanism that has corrosive elements is evidenced during CMAS (Calcium, Magnesium, Aluminum, and Silicon) attack where molten CMAS infiltrates microcracks in the TBC and creates thermal stresses leading to spallation.

Since 1979, the University of Cincinnati has operated a facility capable of accelerated erosion studies on aircraft turbine blade samples at various impingement angles and temperatures up to 1093°C (Tabakoff et al, 1979). Using this facility, it has been shown that impingement angle has a strong influence on the erosion rate of different surfaces (Tabakoff et al, 1995). Walsh et al. reported that erosion rates are also a function of erodent character, temperature, and impact velocity (Walsh et al, 1995). A study by Zaita et al. of the contribution of erosion to tip clearance growth in aircraft engines indicated that erosion effects were a large contributor to efficiency loss over time and a critical parameter in determining engine efficiency degradation (Zaita et al, 1998). It is likely that a critical threshold temperature exists between regimes where erosion is the

dominant degradation mechanism and where deposition becomes critical. Once particulates exceed the temperature where they become molten, agglomeration rates increase with an attendant decrease in blade erosion rates (Wenglarz et al, 2002). Deposition research in aircraft engines has indicated that this threshold for the deposition mechanism in aircraft turbine engines is between 980 and 1150°C (Wenglarz et al, 2002; Toriz et al, 1988; Smialek et al, 1992). Kim et al. looked at deposition in aircraft engines arising from ingestion of volcanic materials (Kim et al, 1993). Their facility consisted of engine components simulating both can-type and annular-type combustors and HP turbines. They found that deposition did not occur below 1121°C. They also reported that deposition rates increased with time as the surfaces became better captors of material and was roughly proportional to concentration given constant temperature and exposure time. However, the conditions of land-based GT engines make the investigations by Kim et al. only marginally useful, particularly since most GT inlet filters will block the majority of particles ingested by the aircraft engines examined in their volcanic ash experiments.

This temperature threshold range is still below the turbine inlet temperature of H-class GT engines. It also falls below the temperature threshold (nominally 1100°C) observed by Wenglarz, where larger fractions of the particulate are molten and therefore stick to the turbine surfaces more easily (Wenglarz et al, 1992; Wenglarz et al, 2002). This temperature threshold dictates that a viable accelerated deposition facility must be capable of studying flow regimes at temperatures significantly above and below 1100°C.

Previous research indicates that the need for an accelerated testing facility exists, and this need will only increase as turbine inlet temperature (TIT) increases with the introduction of new materials technology. Without a good understanding of the depositional mechanisms involved at these higher temperatures, accurate estimates of turbine efficiency during extended service may prove elusive.

Motivations and Theoretical Foundations

The aim of this research is to model the effect of the deposited materials on the efficiency and survivability of the turbine blades themselves. It is possible that though these particles degrade the surface—thereby causing reduced performance through increased heat transfer and turbulence, reduced surface protection by exotic materials, and micro-geometry deformation—their net effect may be to insulate and protect the surface thus improving the overall survivability and long-term performance of the turbine blade beyond what present models predict. Dr Soechting stated that “as an observation, I have seen many parts that had high roughness levels that did not affect the life of the part” (Soechting, 2003). Blade roughness and its accompanying increase in convective heat transfer may not be as detrimental to turbine blade life as presently thought. The insulation of the turbine blade by the deposit layer may be responsible for this presently unexplained phenomenon.

Consider a thermal analysis in one dimension as illustrated in Figure 1. By reducing the turbine blade surface to a semi-infinite flat plate and considering the deposit layer to be non-porous, homogenous, and flat, a model of the possible effect of a deposit layer upon the blade heat transfer may be developed. This simplified geometry is governed only by

a one-dimensional form of the heat diffusion equation using thermal resistances to describe a composite heat transfer system:

$$q_s'' = \frac{(\Delta T_S)}{\left(\frac{1}{h_s}\right)} \qquad q_R'' = \frac{(\Delta T_R)}{\left(\left(\frac{L}{k}\right)_{Deposit} + \frac{1}{h_R}\right)} \qquad (1)$$

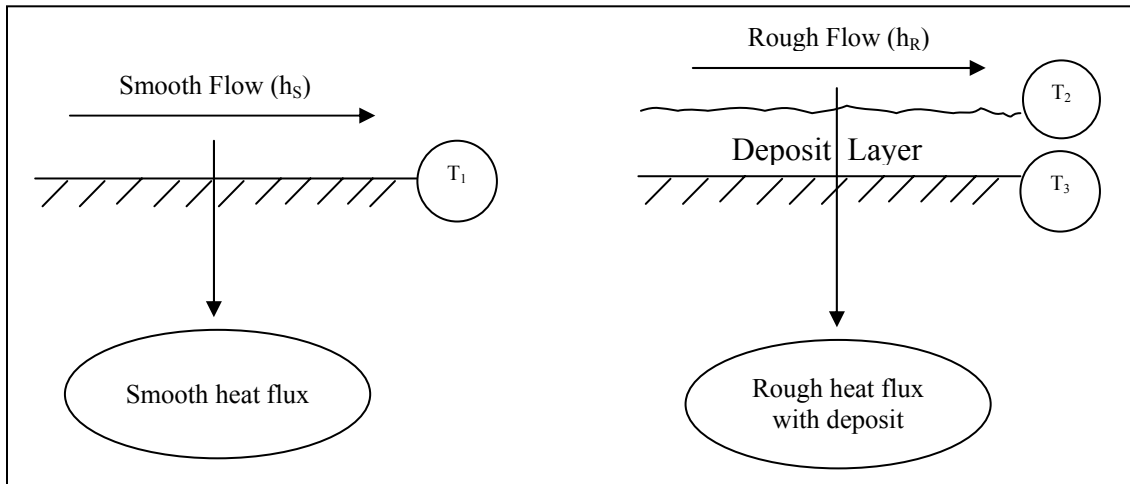


Figure 1: Two flow regimes and subsequent 1-D heat flow analysis

By treating the convection and conduction mechanisms as thermal resistances to heat flow, the overall heat transfer to the turbine blade surface may be modeled as a flow through a composite thermal circuit consisting of a convective resistance and a conductive resistance if a deposit is present. A simple analysis may then be conducted under either of two conditions: (1) the metal substrate has a constant surface temperature; and (2) the cooling capacity—and therefore total heat flow through the material—remains constant. The case of constant surface temperature examines the reduction in required cooling due to the reduction in heat flow through the turbine blade. The

constant heat transfer case examines how a temperature difference may be increased if the cooling capacity of the blade remains constant as the deposit layer thickness increases. This increase in temperature difference could be translated directly into higher operating temperatures, increased efficiency in the turbine, and increased blade life.

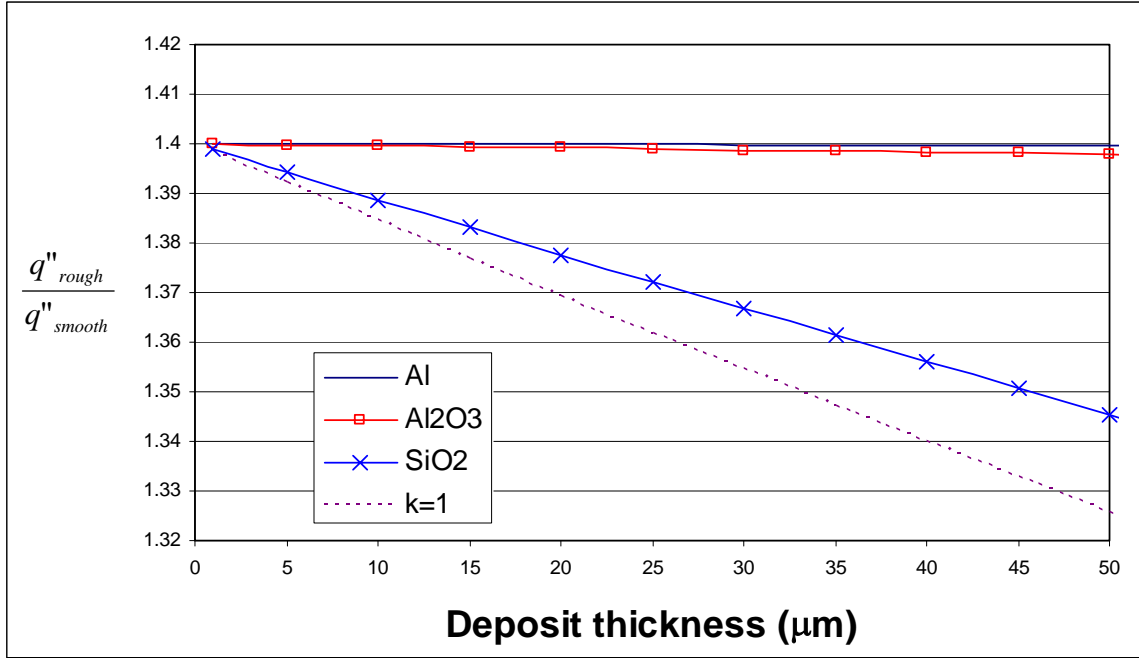


Figure 2: Ratio of heat flow for rough surface to smooth surface as a function of deposit layer thickness for various values of thermal conductivity and $h_s = 800 \text{ W/m}^2\text{-K}$

The first of these conditions—that of constant substrate surface temperature ($T_1=T_3$ in Figure 1, $\Delta T_S = \Delta T_R$ in equation 1)—leads to the following equation:

$$\frac{q''_R}{q''_S} = \frac{1/h_s}{\frac{1}{h_R} + \left(\frac{L}{k}\right)_{Deposit}} \quad (2)$$

Dunn presents a representative estimate of the convective heat transfer coefficient in axial flow turbines, reporting that they lie between 500 and 1600 W/m²-K (Dunn, 2001).

Taking h_R to be 40% greater than $h_S = 800$ W/m²-K (Bons et al., 2001) and then solving for the heat flow ratio produces a relationship between the required cooling capacity and the average thermal conductivity of the deposit material. This resulting trend is illustrated in Figure 2 for several materials common to the turbine environment. The plot illustrates that the deposit layer may be able to suppress the expected increase in heat flux by 5-10% for deposit layers up to 50 microns thick and even more at larger thicknesses.

Though metallic aluminum is included on this chart for comparison, the vast majority of turbine deposits are metallic oxides such as Al₂O₃ and SiO₂. Although this analysis considers the deposit layer to be solid, it is considered likely that these deposits are at least semi-porous, similar to boiler ash deposits (Robinson et al., 2001, pt2). If this is the case, the low thermal conductivity of air would likely drive the composite thermal conductivity of the deposit layer down significantly, regardless of the principal material it is composed of. These factors lead to the conclusion that the region bracketed by the $k=1$ and SiO₂ curves is most indicative of the possible savings in requisite cooling capacity due to deposit growth. There is, however, the possibility that even lower effective thermal conductivity may result from high porosity (since air has a thermal conductivity two orders of magnitude smaller than that of SiO₂ and other solid ceramic materials).

The second case of interest is that of constant cooling capacity. By maintaining heat flow constant as foreign material deposits on the blade surface, a new one-dimensional relation defines the system ($q''_{\text{rough}} = q''_{\text{smooth}}$ and $T_1 \neq T_3$, refer to Figure 1):

$$\frac{\frac{1}{h_R} + \left(\frac{L}{k}\right)_{\text{Deposit}}}{1/h_S} = \frac{T_{\infty,R} - T_3}{T_{\infty,S} - T_1} \quad (3)$$

This relationship examines the possibility that the deposit may allow for a larger difference in freestream to substrate surface temperature than is presently considered possible, thus leading to an overall increase in efficiency similar to the gain made by increasing TIT. Again assuming h_R to be $1.4 h_S$ and $h_S = 800 \text{ W/m}^2\text{-K}$, this condition establishes an operating temperature ratio as illustrated in Figure 3. For deposits on the order of 50 microns thick, approximately 4% of the surface temperature difference from the freestream temperature may be recovered if cooling capacity remains constant. Since the surface temperature is fixed by the thermophysical properties of the substrate, this gain is entirely realized through elevating the freestream temperature. This, in turn, increases the overall turbine efficiency.

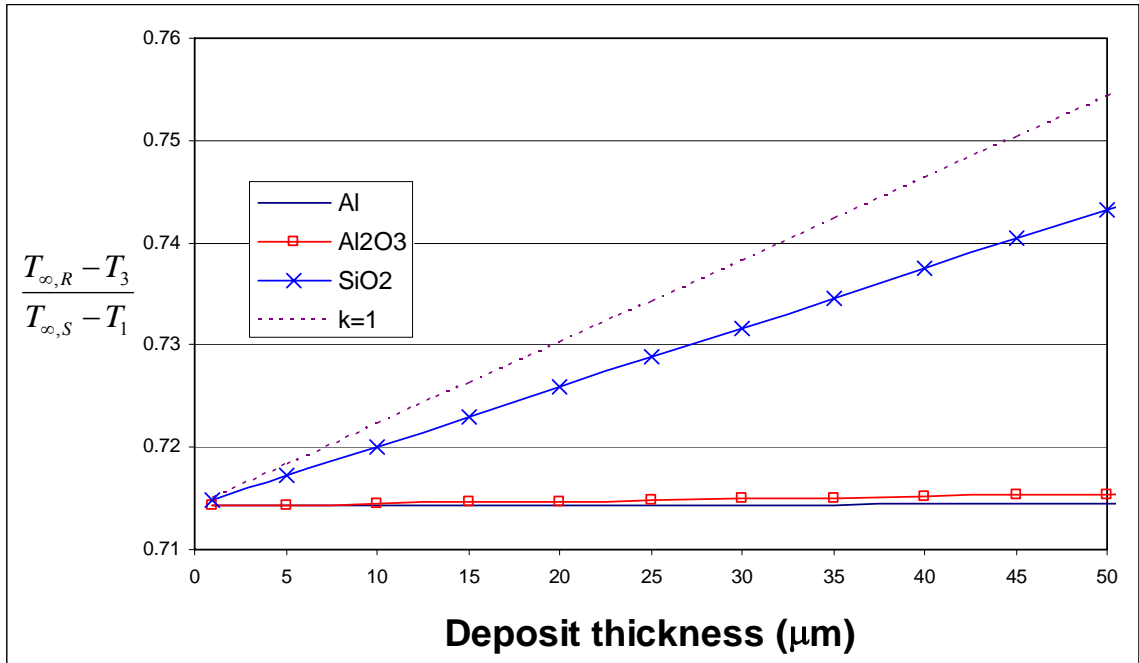


Figure 3: Operating temperature difference ratio as a function of deposit layer thickness for various values of thermal conductivity and $h_s = 800 \text{ W/m}^2\text{-K}$

Though this simple one-dimensional analysis illustrates the possibility of significant effects on operating temperature and heat flow in the turbine blade, the author is unaware of any research into the specific effects of deposit layer thickness and thermal conductivity upon the heat flow into a turbine blade. Though many efforts have been made to characterize aircraft turbine blade thermal barrier coatings (Borom et al, 1996), steam turbine blade erosion (Tabakoff et al., 1995), exposure to volcanic particulate (Kim et al, 1993), the formation of coking deposits in coal power plant combustors (Brandeur et al, 1996), the convective heat transfer increase due to a rough turbine blade surface (Bons, 2002), as well as the thermal effects of deposits in heat exchangers (Robinson et al, 2001, part 2), an extensive literature review revealed no experiments or research designed specifically to explore the conduction properties of the deposit layer typical to

land-based GT engines. Thus the model for turbine blade wear and life prediction can be improved by including information relating to the thermal insulation provided by typical deposits. This work has focused on the preparation of samples of deposits typical to the turbine operating environment, a characterization of the deposit thickness and structure, and the determination of the average thermal resistance change of a turbine coupon due to the development of a deposit layer.

Procedures for Experimentation

Samples of turbine blade material with representative deposits were prepared using a new combustion apparatus that mimics turbine operating conditions by matching the inlet temperature and Mach number of land-based turbines as closely as possible. Research indicates that a minimum threshold near 1090°C exists, below which deposits will not form on turbine blades (Borom et al, 1996). This seems to be the critical parameter to match in experimentation. By matching temperature and Mach number, turbine operating conditions may be mimicked in the test apparatus.

Representative specimens of turbine blade material (including TBC) have been obtained from various turbine manufacturers. These specimens were placed in the flow path of the hot combustion gases and particulate at three discrete angles (90°, 60°, and 30°) from the impinging flow path. These simulate typical angles between the blade surface and the flow path, including stagnation (90°) at the leading edge of a turbine blade where deposition seems to be the most aggressive. Particle streams were injected into the flow at scaled concentrations to approximate total mass throughput parameters for service GT engines. These particles were on the order of 1-80 µm in diameter and composed

primarily of metallic oxides in accordance with similar research published with regard to aircraft GT engine particle ingestion (Dunn et al, 1987; Kim et al, 1993). For simplicity at this stage, no seed material was added to simulate wear from upstream engine parts composed of exotic materials such as Inconel, zirconia, yttria, and other superalloys. This consideration can easily be made by modifying the particulate mixture in future investigations.

Once a specimen was obtained, the surface roughness of the deposit was measured using a profilometer. Afterwards, due to the destructive nature of further tests, samples were alternately set aside for thermal resistance testing or secured to the substrate using an epoxy resin designed to penetrate microscopic pores. This epoxy maintained the structure of the deposits and allowed them to be cut into cross-sections for SEM analysis of the internal structure. These cross-sections were further analyzed using x-ray diffraction techniques to determine their chemical composition.

The thermal model of the deposit was developed using a direct measurement of the thermal resistance offered by the deposit. Specimens not slated for cross-section analyses were exposed to a constant heat flux using a flat flame methane-hydrogen burner. By measuring the temperatures of the deposit surface and the rear substrate surface as well as the flux through the entire specimen, an estimate was made of the thermal resistance of the entire specimen (turbine base material, TBC, deposit). This was compared to the thermal resistance of blank samples without deposit layers whose thermal resistance was measured in like manner.

Scanning electron micrographs of the deposit cross-sections were used to begin to establish a theoretical model of heat conduction in the deposit layer. By coating a sample with epoxy and allowing it to harden, cross-sectioned samples may be examined to determine the stratification (if any), porosity, and tortuosity of the deposit. These parameters coupled with a chemical composition estimate obtained through x-ray diffraction analysis can yield a theoretical model of heat transfer through the deposit layer similar to those reported by Robinson et al in their studies of boiler scale in heat exchangers (Robinson et al, 2001, part 1). Though this work presents a partial development of this model, it has not yet been completed or validated.

Summary

This research aims to answer the basic question of whether the conduction characteristics of deposit layers may be neglected in thermal studies of turbine blades as is presently done in most industrial and scientific experimentation. This goal was accomplished by simulating a depositional environment, coating turbine blade material samples with a deposit layer similar to those found in power plant turbines, and then testing the deposit layer's thermophysical properties. These property tests determined porosity and stratification (by SEM analysis), thermal resistance (using a heat conduction experiment), and chemical composition (using x-ray diffraction techniques). Using these tools, an estimate of the thermal resistance provided by a deposit layer to an operational turbine blade can be made, thus allowing a more accurate prediction of turbine blade life than was previously possible.

Chapter 2: An Accelerated Testing Facility

In order to study the structure and thermal properties of deposits forming on first stage high pressure (HP) turbine vanes and blades, an experimental facility was constructed to duplicate conditions in the blade leading edge zone where deposition tends to be the heaviest (Bons et al, 2001). This facility attempts to replicate the chemistry and structure of deposits occurring on turbine blades after 10,000 hours service in 4-hour accelerated tests. The facility is capable of matching the Mach number and flow temperature in the first stage of the turbine while also providing a means of varying the impingement angle of the flow on the sample and the particulate concentration in the flow. A schematic of the facility is shown in Figure 4.

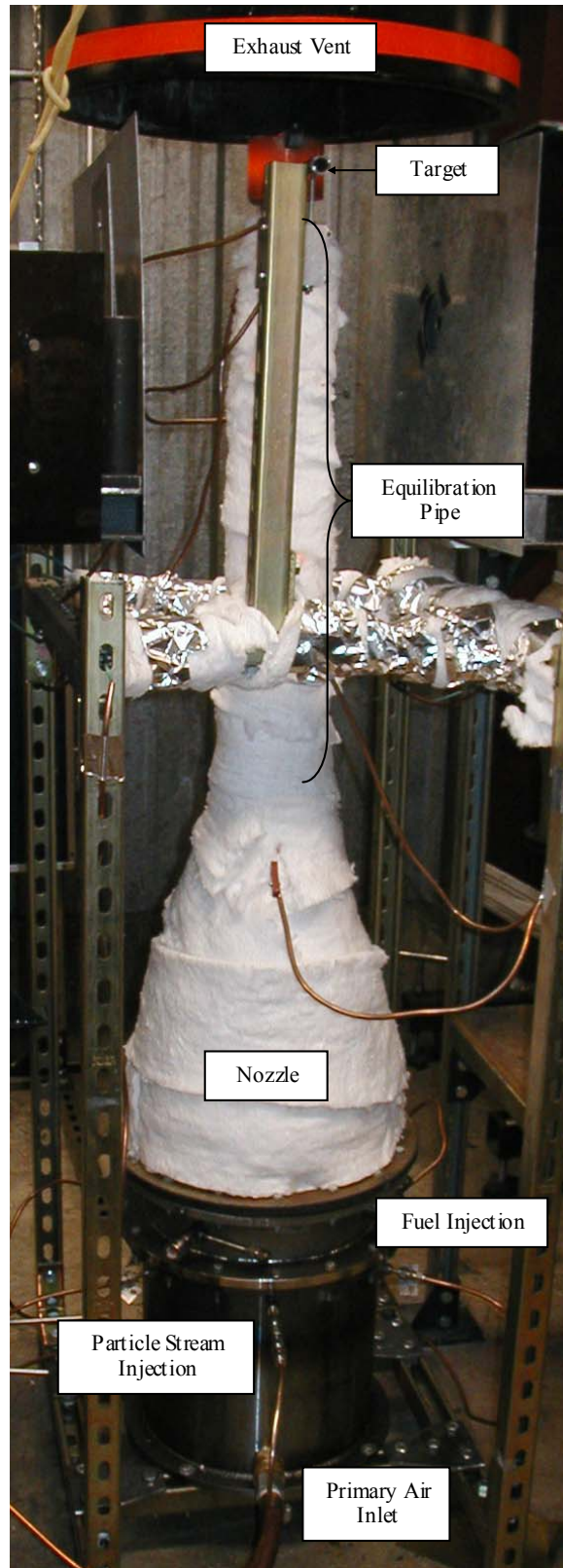


Figure 4: Accelerated testing facility

The Combustor

To properly simulate deposition mechanisms in the HPT, the gas turbine combustor exit flow conditions must be duplicated in the laboratory. The critical variables for an accurate simulation include: flow temperature, Mach number, and impingement angle, as well as particle size, chemistry, and loading. Gas (and particulate) temperature is important since it influences the state and thus susceptibility for deposition of molten particulates in the flow (Wenglarz, 2002). For particle sizes in excess of 1 to 2 microns, the primary means of deposition is inertial impaction, making impingement angle and particle velocity (flow Mach number) critical parameters governing the force of impact and the momentum transfer during a collision with the blade surface. Below one micron, other processes including turbulent eddy diffusion, thermophoresis, and Brownian diffusion dominate the deposition mechanism (Wenglarz et al, 2002).

One flow parameter that is not simulated in this test facility is static pressure (the deposition occurs at pressures less than 15kPa above atmospheric pressure). This is consistent with other deposition test facilities that operate at significantly lower pressures than those found in a GT (Tabakoff et al, 1995; Wenglarz et al, 1990). The consensus from these and other studies (Kim et al, 1993; Borom et al, 1996) is that particle temperature, concentration, and residence time are the necessary parameters for proper simulation, not static pressure.

As for matching the particulate loading in the gas stream (parts per million weight or ppmw), Wenglarz describes various experiments where particulate concentration and service time seemed to tradeoff between each other (Wenglarz et al, 2002). Turbines exhibited large deposits or could even be driven to failure either by high particle loading at low service time or low particle loading for long periods (Wenglarz et al, 2002). This suggests that a throughput mass factor may be the key parameter and the time to produce a surface deposit could be reduced by increasing freestream concentration of particulate. The validation of this hypothesis was the subject of initial investigations in this work.

Deposition can occur from a variety of mechanisms, both internal to the GT (e.g. dirty fuels or eroded components) and from the environment (airborne sand, salts, etc...). The focus of this study is the simulation of airborne particulates ingested into a natural gas burning engine. In the laboratory, this is done by seeding a natural gas combustor with high concentrations of airborne particulates. A description of this facility follows.

The primary air stream is injected into the steel base of the natural gas combustor where it is first dispersed by passing through a volume of marbles and then straightened through a 5cm tall honeycomb section. At this point, natural gas is injected into the flow via four stainless steel fuel injectors. The detailed chemical composition of this fuel is given by Murray, but it primarily consists of CH_4 (Murray et al, 1998). The combusting flow then enters a 20° conical axisymmetric nozzle with a 370:1 inlet to exit area ratio. The elevated Mach number at the nozzle exit is maintained through a 0.9m long pipe leading to the test coupon where entrained particles are brought up to 95% of flow speed and

temperature. The length of this pipe was dictated by the estimated residence time required for particles of up to 40 micron diameter to come to thermal and velocity equilibrium with the gas flow at the nominal test conditions. The length to diameter ratio for this equilibration pipe is 50.

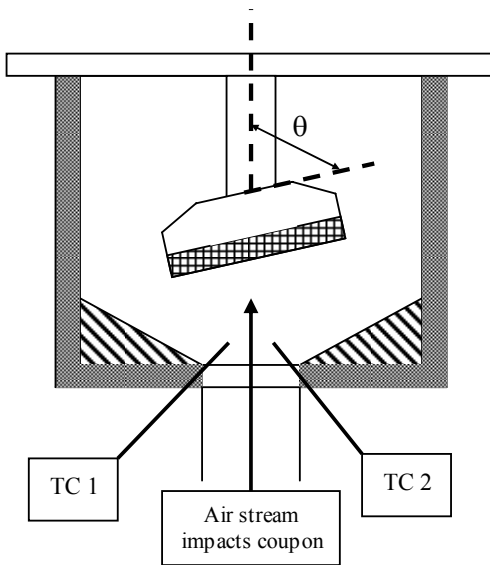


Figure 5: Cut-away of target area (TC1 and TC2 show flow thermocouple placement).

The flow exits this equilibration pipe as a turbulent jet and impinges on the target coupon located 2-3 jet diameters from the pipe exit (Figure 5). The jet exit Mach number for the experiments reported in this study has been set to match the typical inlet Mach number range (0.2-0.4) for a first stage turbine blade row, though the capability exists to operate at Mach numbers twice this high. The fixture holding the coupon can be oriented at a 30, 45, 60, or 90° angle to the flow path, allowing the simulation of various impingement angles found in a turbine flowpath as the flow stagnates against the leading edge and then sweeps around the airfoil.

Particulate

In order to match the high temperatures characteristic of the HP turbine, the combustion section and all other downstream components are constructed of Inconel 600 and 601 alloys for maintenance of a high temperature flow without necessitating a cooling jacket. Inconel 600 and 601 have a high lower melt temperature (1350°C) which allows experiments to operate up to a mean temperature of 1150°C with maximum temperatures of 1200°C. Provisions have been made for increasing this maximum operating temperature to 1350°C with a steam cooling jacket around the equilibration pipe. For now, system temperatures are maintained using ceramic insulation around the entire combustion facility.

Simulation of a particulate-laden flow is achieved by seeding particles into the air stream by means of a secondary air flow system. Though the primary use of this facility to date has been to model the ingestion of foreign particles at the GT inlet, this facility could also be used to examine the impact of burning “dirty fuels” or excessive internal erosion in GT engines. By seeding the air flow with the proper mixture of ash, chemical impurities, GT engine material, or other elements, this facility could be used to simulate the burning of biomass, coal, heavy fuel oils, or any other of a variety of alternative fuels as well as internal erosion by ingested particles or the break-up of particles deposited upstream of the turbine.

In order to examine the case of airborne particle ingestion from the atmosphere, an understanding of the typical particulate content of the atmosphere was needed. The particulate content of a typical urban atmosphere consists of a bimodal distribution

centered at 0.5 and 10 microns (Seinfeld et al, 1998; Finlayson-Pitts et al, 1999). The finer of these two distributions is comprised mostly of ignition losses and the solid-state products of multi-phase chemical reactions in the atmosphere (sulfates, nitrates, ammonium compounds). The coarse particle regime consists primarily of particles that have been broken down from macro-scale sources by mechanical processes such as erosion, sea spray, and dust aeration by traffic. The chemical distribution of these latter particles can vary greatly from region to region depending on the dominant physical environment. In urban and desert locations where many GT engine plants are located, these coarse particles are distributed nearly identically to standard crustal and soil elements.

Borom et al. confirmed that a “globally generic” chemical composition called CMAS (Ca-Mg-Al-Si) could be considered when studying the deposition of environmental particulate to air plasma sprayed (APS) TBC (Borom et al, 1996). Furthermore, the distribution of materials in these deposits resembles generic weight percent distributions for the earth’s crust (Ford, 1954) (see Table 1). This suggests that simply injecting common dirt into a combustion facility would provide the correct ingredients and relative concentrations for the formation of deposits in a turbine so long as the particle sizes were controlled to those common to a turbine environment.

Table 1: Crustal & seed particulate composition as percent by weight. SEM analysis lists element as N/A if none was detected above measurement noise. All Iron detected by SEM assumed Fe₂O₃ oxide. “Other Alkalis” detected by SEM consisted entirely of Potassium. SEM assay representative of multiple assays.

	Crustal Composition (Ford, 1954)	Manufacturer Assay of Seed Particulate	BYU SEM Assay of Seed Particulate
SiO ₂	59.8	68.5	60.2
Al ₂ O ₃	14.9	16.0	4.5
CaO	4.8	2.9	13.7
MgO	3.7	0.8	N/A
Other Alkalies	6.2	4.6	7.3
Fe ₂ O ₃	2.7	4.6	10.7
FeO	3.4	negligible	negligible
H ₂ O	2.0	0.0	N/A
Ignition Losses	N/A	2.7	N/A

Though the majority of airborne particles are concentrated in the range of 0-20 microns, particles up to a size of 80 microns can often be found in small amounts. This forms the upper limit on what can be expected in reasonable abundance within the atmosphere.

However, land-based GT engines employ inlet filters that trap out a significant portion of these particles. Many such filters are capable of blocking nearly all particulate from entering the GT engine when newly installed, but degradation over time can cause these filters to allow passage of particulate in steadily increasing amounts (Fintland, 2003).

Even after significant service, most mid-grade filters are capable of filtering out particles sized 20-80 microns and a significant portion of particles smaller than 20 microns, but the arrestance of particles in excess of 4 microns in size will often decrease more rapidly than the arrestance of the bulk of ambient particulate which lies near 1-2 microns in size (Fintland, 2003). It might also be argued that even if large particles are ingested through the air filter, they will be pulverized as the gas flows through the compressor to the turbine. While this is generally true, Dunn et al. also reported that both bypass and ECS

air in aircraft systems showed measurable amounts of particulate in excess of 20 microns in size despite having passed through the aircraft compressor (Dunn et al, 1987a).

Seed particles were selected to match the typical particulate size and chemistry found in the atmosphere. Contact with Air Filter Testing Laboratories, Inc. led to the selection of a particle test mixture used in the characterization of GT inlet filter performance. The dust selected conforms to the ASHRAE (American Society of Heating, Refrigeration, and Air Conditioning Engineers) test standards for size and is representative of real chemical compositions as it is collected from the atmosphere rather than artificially mixed. The chemical composition of this seed particulate is given in Table 1 while the mass-percent size distribution is shown graphically in Figure 6. Note that our independent SEM assay of the particulate showed a different chemical composition than the manufacturer-provided assay and did not detect Mg (a prime component of CMAS) in appreciable quantities.

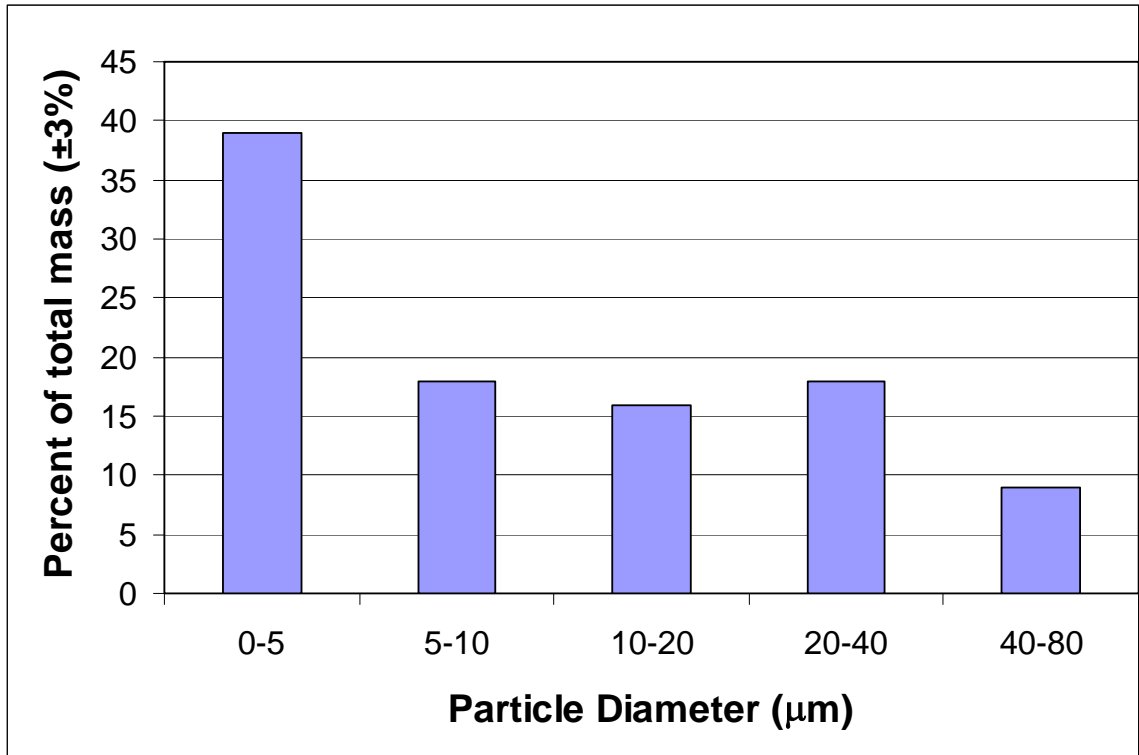


Figure 6: Seed particle size distribution by mass

Approximately 9% by mass of this dust exceeds the size limit for 100% entrainment by the gas flow in the equilibration pipe. Though thermal equilibrium (analyzed using a lumped capacitance model) is achieved for all particles in about 20% of the time required for velocity equilibrium, large particles will not achieve velocity equilibrium (defined as 95% of gas velocity) before impingement. By applying the Stokes Flow assumptions on viscous flow, the entrainment of particles in this facility can be modeled with the following relationship:

$$\rho_p \frac{\pi}{6} d_p^3 \frac{dv_p}{dt} = 3\pi\mu d_p (v_f - v_p) \quad (4)$$

predicts that particles larger than approximately 40 μm (corresponding to the size category for the largest particle diameter as shown in Figure 6) will not achieve the full 95% of flow velocity to be considered entrained with the flow. Because of the velocity gradients which are present in the HPT, it is likely that this will not adversely affect the ability of the accelerated deposition facility to duplicate the deposit mechanisms under study.

In order to represent the flow conditions typical of ingestion of particulate in the primary air stream in a GT engine, part of the main air flow in the combustion facility (20-40%, depending on flow conditions for the test) is branched from the main air system upstream of the combustor. This flow enters a glass bulb into which particles are steadily injected using a glass syringe. The syringe pushes particulate into the glass bulb where it is entrained into the air stream. The glass bulb is vibrated by mechanical agitation at 60 Hz. in order to ensure a continuous flow of particles in the smallest agglomerates possible. The feed rate of the syringe can be adjusted to control the overall mass concentration of particulate in the flow. This report focuses on experiments with particle concentrations from 60 to 280 parts per million weight (ppmw). Particle loading for a typical GT with adequate filtration is initially 1-5% of ambient particulate content (Fintland, 2003). This value can reach as high as 25% under adverse conditions such as sandstorms, filter deterioration during regular service, or high smog. Average ambient content of 10-micron particles (PM_{10}) in an urban environment is $300 \mu\text{g}/\text{m}^3$ (Seinfeld et al, 1998) or about 0.244 ppmw. Filtering to 1-25% of this ambient level yields 0.002-0.061 ppmw in the turbine intake. Thus, 60 and 280 ppmw for 4 hours yields roughly the same

throughput particulate mass as 0.024 and 0.112 ppmw for 10,000 hours. The particle loading is determined by weighing the particulate remaining in the syringe at the conclusion of the test and comparing it to the total weight measurement made at the start. This difference in particulate mass, divided by the testing time and normalized by the massflow rate of air yields the required ppmw estimate. Uncertainty in the particle concentration measurement was <5 ppmw.

Instrumentation

Test conditions are monitored real-time using mass flow and temperature sensors. Air flow is metered by a choked flow orifice plate. A Dan Foss Fluid Components International model CMF-D mass flow meter used for calibration purposes showed good agreement (error <4% full-scale) with the orifice plate measurement. The fuel flowrate is measured with a rotometer and line pressure measurement. The two massflow measurements are compared to determine combustion stoichiometry. Uncertainty in total mass flow was 4% at flow regimes of interest. The flow temperature is measured using two S-type thermocouples located in the jet exit, just upstream of the target coupon (Figure 5). These 0.13mm bead diameter thermocouples are held in the flow with ceramic supports. The thermocouples are positioned so that they do not view any low temperature surfaces, thereby keeping the radiative temperature errors to within 3°C. Because the convective mechanism at the Mach numbers of interest is quite high, the convective error on temperature sensing is also quite low. Overall error is less than 15°C at 1150°C. Metal surface temperatures are also monitored at various points along the exterior of the combustion facility as a precaution against overheating the combustor.

Using these measurements, the Mach number was calculated using the Ideal Gas Law relation for the speed of sound:

$$M = \frac{\dot{m}}{\rho_{gas} A_{exit} (\sqrt{\gamma RT})_{gas}} \quad (5)$$

Gas properties for air-combustion (nitrogen-rich) gases were used ($\gamma=1.3$).

Samples of turbine blade materials with APS TBC were provided by several GT manufacturers for testing in this facility. In order to respect proprietary concerns of the manufacturers, strict source anonymity has been maintained for all data presented in this publication. The materials were modified as necessary to fit into the 2.5cm diameter test coupon tray. The specimens were typically 4mm thick with 100-200 μm of TBC on the high temperature alloy substrate.

Chapter 3: Validation of the Structure of Deposits Formed in Accelerated Testing

The primary objective of initial experiments was to validate the use of accelerated deposition testing. This is done by comparing specific features from accelerated deposition coupons to deposit features found on in-service hardware. The criterion for determining whether the two modes of deposit formation are indeed similar rests upon thermodynamic considerations. Specifically, if an assessment of the deposits would yield comparable effects on turbine performance, then the deposits are considered to be “similar”. Deposits alter the blade thermodynamics through two primary mechanisms: convection and conduction. Convection is influenced by changes in surface roughness. Bons tested scaled models of actual turbine deposit roughness and found 20-40% increases in convective heat transfer (Bons, 2002). Several roughness statistics were suggested as possible correlating parameters for the observed increase in heat transfer. Thus, if the deposits generated in this accelerated deposition facility have a statistically similar character to those found on actual in-service hardware, they would be considered “similar”. Accordingly, surface topology measurements were made to allow statistical comparisons of roughness.

Deposits also form an insulating layer over the TBC, thus reducing heat flow to the metal substrate. This conduction mechanism is governed by the deposit thickness, chemistry, and structure. As such, measurements were made of the deposit internal structure and chemical composition using SEM and X-ray spectroscopy. The results of these two studies are presented below. Following this, some remarks are made regarding observed variations in deposit characteristics with impingement angle, particulate concentration, and gas temperature.

Topography

The most obvious measure of similarity is a visual inspection of real turbine blade deposits and those created under accelerated conditions. Early examinations at 10x magnification (Figure 7) indicated the likelihood that accelerated samples were practical approximations of the deposits seen on turbine blades. These cursory examinations led to more in-depth investigations into the surface characteristics of the deposits created in the accelerated test facility.

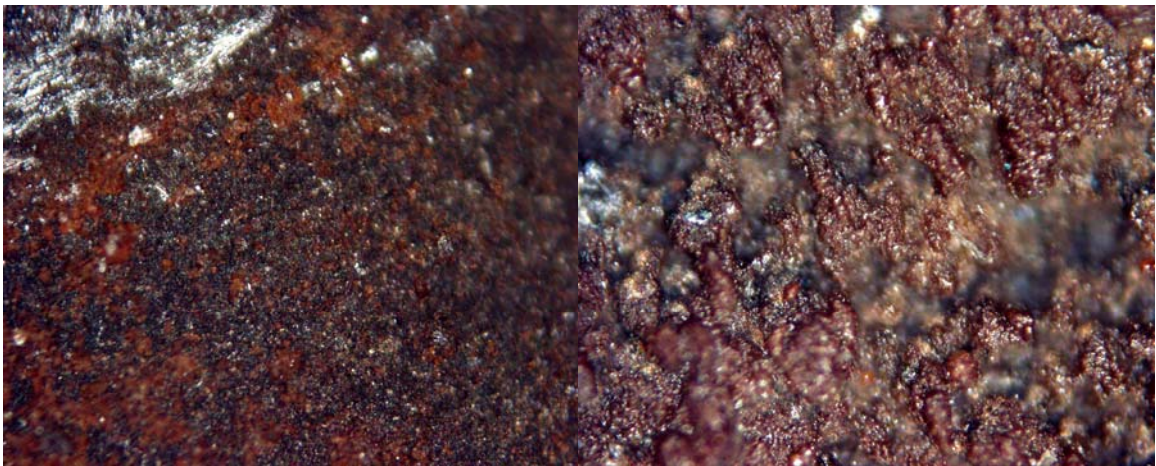


Figure 7: Surface pictures of deposits on service turbine blades (left) and accelerated samples (right) show similar structure, color, and coverage. Pictures were taken at 10 times magnification. The above specimens are approximately 3mm x 3mm.

Surface roughness in turbines is governed by an imposing list of parameters including: service hours, cycles, operating temperature, and environment. Bons et al reported significant variations with blade location and surface degradation mechanism (spallation, deposition, or erosion) as well (Bons et al, 2001). Traditionally, roughness is characterized by its statistics (e.g. Ra, Rt). These statistics can then be used with empirical correlations to estimate changes in skin friction or convective heat transfer (Blair, 1994; Boynton et al, 1993). With such a rich parameter space, it would be unproductive to try to match a specific surface topology from a serviced turbine to that obtained in the accelerated deposition test facility. Instead, statistical comparisons can be used to show that surface formations have similar character and thus would influence performance (e.g. convective heat transfer) in a similar way.

A Hommel Inc. T8000 surface measurement system was used to make 3D surface topology maps of a variety of surfaces. The Hommel uses a $1.5\mu\text{m}$ radius diamond-tipped conical stylus to follow the surface features for a given part. The instrument can measure a total vertical range of 1.6mm with a precision of 75nm. 3D surfaces are constructed from data taken every 5 to $10\mu\text{m}$ on a rectilinear grid (typically 4mm square).

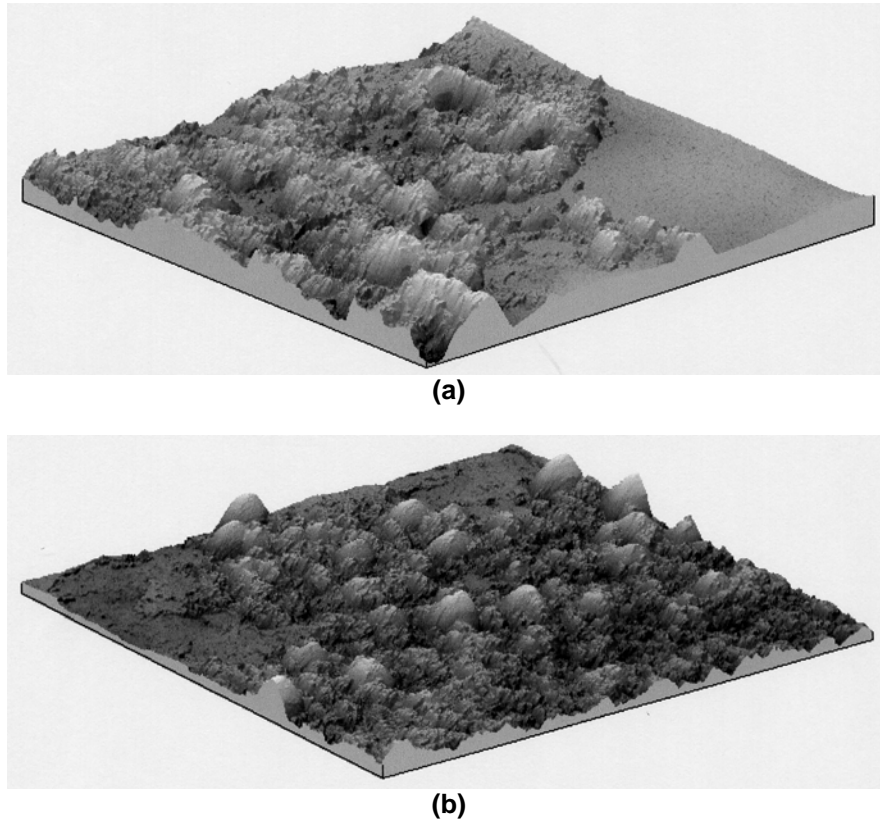


Figure 8: Surface map of deposits from (a) 1st stage turbine with 25,000 hours and (b) accelerated deposit surface after 4hrs at 60ppmw. Both maps are 4mm x 4mm with approximately the same vertical scale.

Figure 8 shows Hommel surface maps of two surfaces. Figure 8a is from a first stage turbine blade with 25,000 hrs of service. The topology map was taken at roughly 60% chord and 30% span on the blade suction surface, a region with obvious brownish deposits. Figure 8b is an accelerated deposition coupon that was tested for 4 hours at 60ppmw ($T = 1150^{\circ}\text{C}$ and $M = 0.33$). The coupon was oriented for stagnation flow (impingement angle = 90°), but the surface map shown was taken at the edge of the coupon where the flow was more tangential to the surface of the coupon as the impinging

jet stream turned about the edges of the target. The strong similarities between the two images are reinforced by a review of their surface statistics (Table 2). Also included in Table 2 are statistics from various accelerated coupon tests and numerous serviced hardware. Though there are wide ranges of statistics for both the accelerated and serviced deposits, the ranges overlap noticeably. Thus, from a convective heat transfer standpoint, the accelerated deposits are considered “similar” to those found in actual serviced hardware.

Table 2: Roughness statistics for accelerated and serviced deposits.

Surface Type	Ra [μm]	Rt [μm]	α_{rms} [deg]	S_w/S	Λ_s
<u>Accelerated</u>					
<u>(4hr test)</u>					
60ppmw, at coupon edge (Figure 8b)	28	257	29	1.43	13
280ppmw, 90deg impingement	32	260	16.5	1.12	82
280ppmw, 45deg impingement	10	107	13.7	1.06	180
280ppmw, at coupon edge	38	249	18	1.11	87
<u>Serviced Hardware</u>					
25000hr blade (Figure 8a)	32	240	27	1.36	22
22500hr blade	41	296	24	1.24	36
<1000hr blade	19	394	18	1.11	77
24000hr vane	17	220	15.8	1.09	134

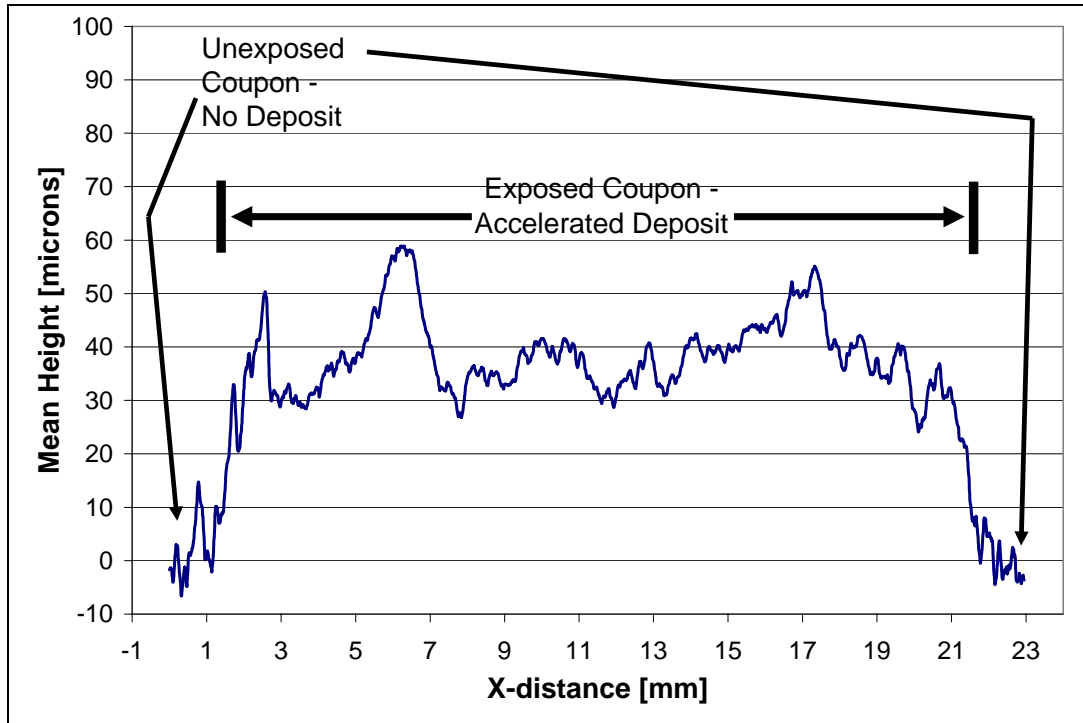
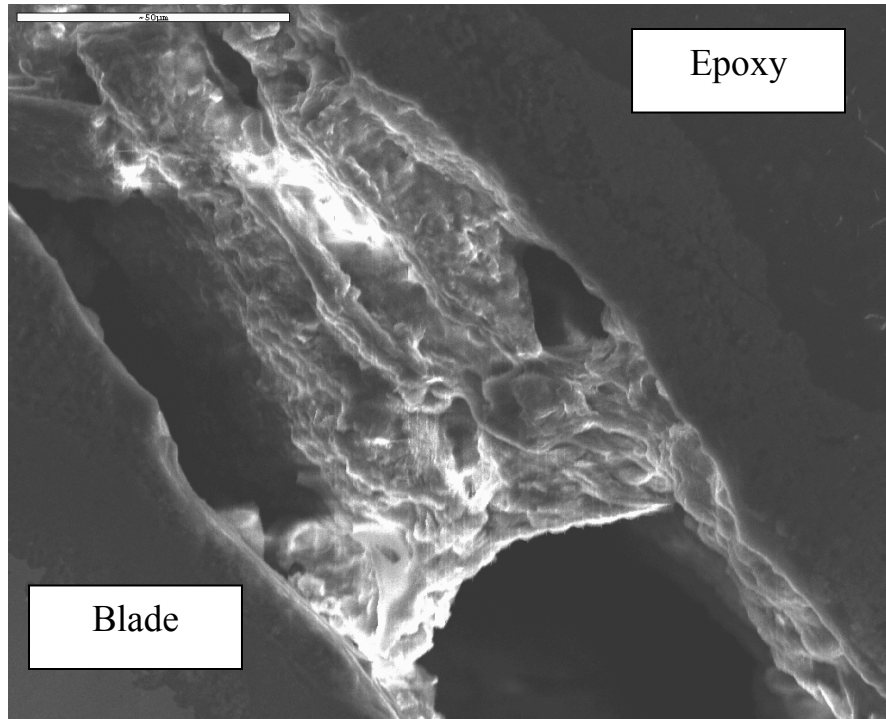
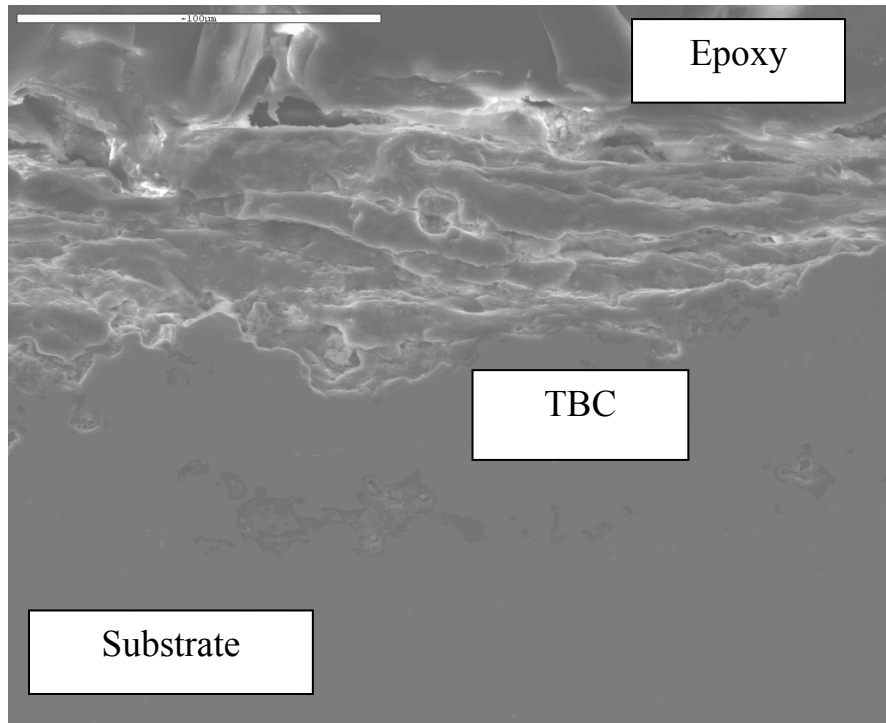


Figure 9: 23mm long surface trace across accelerated deposit test coupon. Vertical scale (units are microns) exaggerated for clarity. 1mm on either end of trace is unexposed TBC surface with no deposits.

The typical thickness of deposits in the accelerated test facility can be seen in Figure 9 which shows the average of 800 profilometer traces across the test coupon. The ends of the trace are unexposed TBC, so the average deposit thickness can be measured relative to this reference height. The deposits in this coupon appear to be roughly 50 μ m thick, though the actual amount of deposit may be greater since the underlying TBC experiences some degradation during testing. A weight measurement of this test coupon before and after accelerated deposition showed an increase due to deposition corresponding to 0.04 grams per square mm of exposed coupon surface.



(a)



(b)

Figure 10: SEM cross-section of (a) a 16000-hour service blade with 50-μm metering bar at top left and (b) an accelerated deposit specimen with 100-μm metering bar at top left

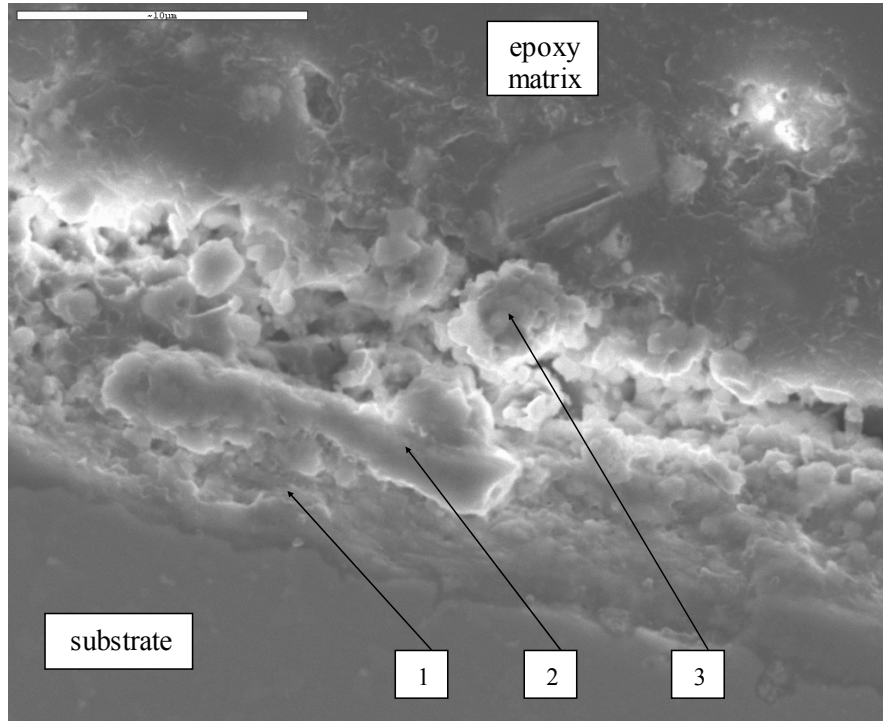
Internal Structure & Chemical Composition

When decreasing the length of exposure by three orders of magnitude, it is natural to question whether the deposition process has fundamentally changed. Though the external surface structure of accelerated deposits may bear resemblance to deposits found on turbine blades with over 10,000 hours service time, in terms of internal heat conduction it is critical to determine whether the internal structure and chemical composition of the deposit is similar as well. To this end, scanning electron microscopy (SEM) was used with both the deposits formed in this accelerated facility and samples obtained from Standard Aero Inc., a third party turbine servicing corporation. Since the turbine hardware available for cross-section did not have thermal barrier coating (TBC), comparison was also made with limited TBC-coated SEM data available in the literature.

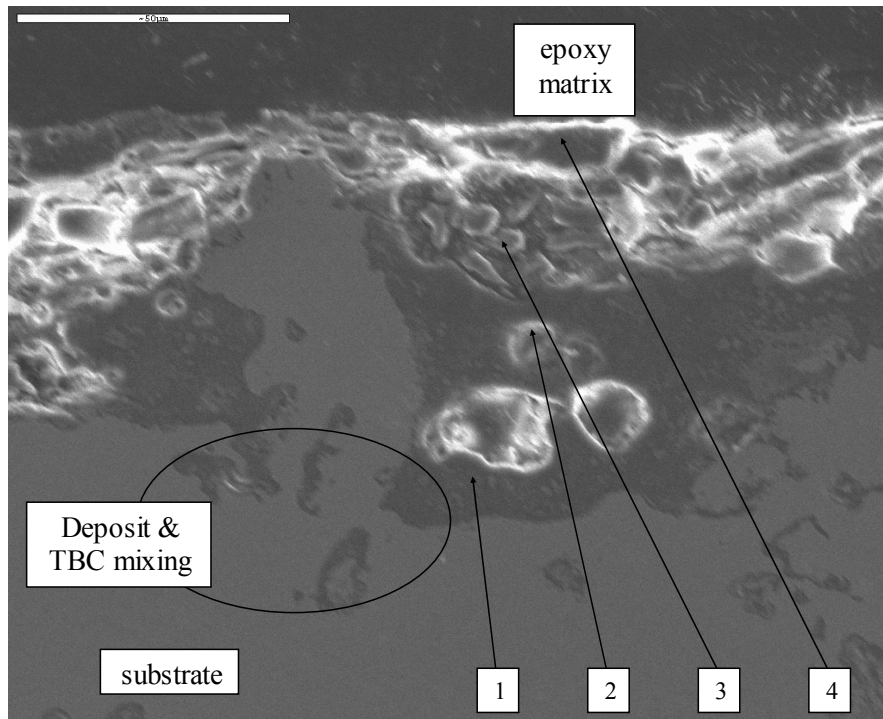
To prepare the specimens for SEM analysis, each test coupon (or blade) was first potted in epoxy resin to prevent dislocation of the deposit during sectioning. Sections were then made and polished to 10 microns. Figure 10 shows side by side SEM comparisons of these microstructures. Figure 10a is from a non-TBC coated blade with 16,000 hours service while Figure 10b is from a 4-hour accelerated deposit on a TBC-coated coupon at $T = 1150^{\circ}\text{C}$, $\theta = 90^{\circ}$, and $M = 0.33$. In both figures, the deposit is sandwiched between the epoxy (on top) and the turbine surface (on bottom). Elongated structures running parallel to the blade surface are evident in both SEM pictures. Another set of comparisons is shown in Figure 11a (non-TBC coated turbine blade with 25,000hrs) and Figure 11b (4-hour accelerated deposit on a TBC coupon at $T = 1150^{\circ}\text{C}$, $\theta = 45^{\circ}$, and $M = 0.33$). The 100-micron thick sample shown in Figure 10(b) and the 50-micron thick

sample shown in Figure 11(b) are of the same order magnitude in size as actual turbine blade deposits shown in Figures Figure 10(a) and Figure 11(a).

Other microstructures including pitting and grain sintering were also observed in both turbine blade and accelerated specimen cross-sections. Since the serviced hardware used in this comparison did not have TBC, comparison was also made with the SEM analysis in Borom et al. (Borom et al, 1996). This study of serviced venturi and turbine shrouds with TBC showed significant mixing between the coating and the deposit. Figure 11b shows a region (circled and labeled) where TBC constituents were found to penetrate into the deposit and vice-versa using x-ray spectroscopy.



(a)



(b)

Figure 11: SEM cross-section of (a) 25000-hour service blade with 10- μ m metering bar and (b) an accelerated sample with 50- μ m metering bar

Table 3: Relative abundance by percent weight at various points as noted in Figure 11. Table (a) matches Figure 11(a) and table (b) matches Figure 11(b). N/A denotes elemental counts below the noise threshold of the instrument. Percentages based only on elements detected above SEM noise threshold.

(a)

service blade point	Common Elements percent weight								
	CaO	MgO	Al ₂ O ₃	SiO ₂	Fe ₂ O ₃	TiO	Cr ₂ O ₃	ZnO	Na ₂ O
1	0.0%	N/A	28.0%	4.1%	20.2%	N/A	25.7%	20.2%	1.8%
2	6.0%	N/A	20.8%	3.4%	26.1%	N/A	23.2%	19.2%	1.3%
3	5.1%	N/A	23.8%	3.8%	35.5%	N/A	11.7%	18.4%	1.7%
Average	3.7%	N/A	24.2%	3.8%	27.3%	N/A	20.2%	19.3%	1.6%

(b)

accelerated sample point	Common Elements percent weight								
	CaO	MgO	Al ₂ O ₃	SiO ₂	Fe ₂ O ₃	TiO	Cr ₂ O ₃	ZnO	Na ₂ O
1	16.2%	N/A	8.4%	59.6%	9.9%	5.8%	0.0%	N/A	N/A
2	27.4%	N/A	3.7%	37.4%	16.6%	9.3%	5.6%	N/A	N/A
3	7.6%	N/A	8.4%	32.2%	20.2%	10.9%	20.7%	N/A	N/A
4	26.7%	N/A	N/A	56.3%	10.9%	6.1%	0.0%	N/A	N/A
Average	19.2%	N/A	6.8%	45.6%	14.1%	7.9%	6.5%	N/A	N/A

With the specimen cross-sections in the polished state, they were also suitable for x-ray spectroscopy measurements. X-ray spectroscopy was used to determine the materials most likely to deposit on the turbine blade surface and compare this to the composition of the seed particles and the deposits on real turbine blades. This analysis is also critical to detecting stratification (if any) within the deposit. Some results of the x-ray spectroscopy are shown in Table 3 for various locations noted on Figure 11. The deposits found on serviced turbine hardware are primarily composed of Ca-Mg-Al-Si (CMAS) as noted by Borom et al. (Borom et al, 1996). Since these elements were nearly all (with the exception of Mg, Table 1) present in the particulate used in this accelerated experiment, it is not unexpected that they also appear in the deposits formed. Table 3 shows the relative abundance of the notable constituents of the deposit layer. Abundances in Table 3 are given in weight percent of the most common oxide of detected nuclei. Only those nuclei detected above the noise threshold of the SEM are considered in calculating weight

percent. Of the elements in CMAS, Mg is conspicuously absent. Mg was not detected in significant quantities in either the turbine blade deposit or the accelerated sample. As noted in the Table 1 heading, the manufacturer assays for the seed particulate indicated the presence of Mg but SEM assays at BYU failed to detect Mg above the noise of the sampling. This is due in part to the SEM apparatus used on the BYU campus which is not equipped to detect small quantities of Mg above the background noise inherent in x-ray measurements. The SEM used on the BYU campus incorporates a Beryllium (Be) filter. Detection signals of all chemical elements of smaller atomic number (4 and below) are completely filtered out of the chemical constituent assay. This filter also significantly reduces the strength of detection signals from elements only marginally larger than Be. Since Mg is both the smallest atomic constituent in CMAS (Mg = 12; Al = 13; Si = 14; Ca = 20) and is also the least abundant by mass, it is entirely possible that the BYU SEM was incapable of distinguishing the Mg signal from the noise of an x-ray assay.

For the turbine blade sample, the absence of Mg could be the result of specific environmental fluctuations. Note also that Ti is evident in accelerated samples though only a small amount of Ti was detected in the initial SEM assay and none was reported by the particulate manufacturer. Finally, Zn and Na are evident in the turbine deposit but were not in significant quantities in either the seed particulate or the accelerated deposit. These could again be the result of the unique chemistry of the ambient particulate mix in the turbine blade operating environment. Note that with the exception of Mg, the mass distribution of oxides in the accelerated sample approximate those reported by Borom et al. for desert deposit samples in aircraft engines (e.g. CaO = 28.7%, MgO = 6.4%, Al₂O₃

= 11.1%, SiO₂ = 43.7% (Borom et al, 1996)). This comparison is made clear graphically in Figure 12.

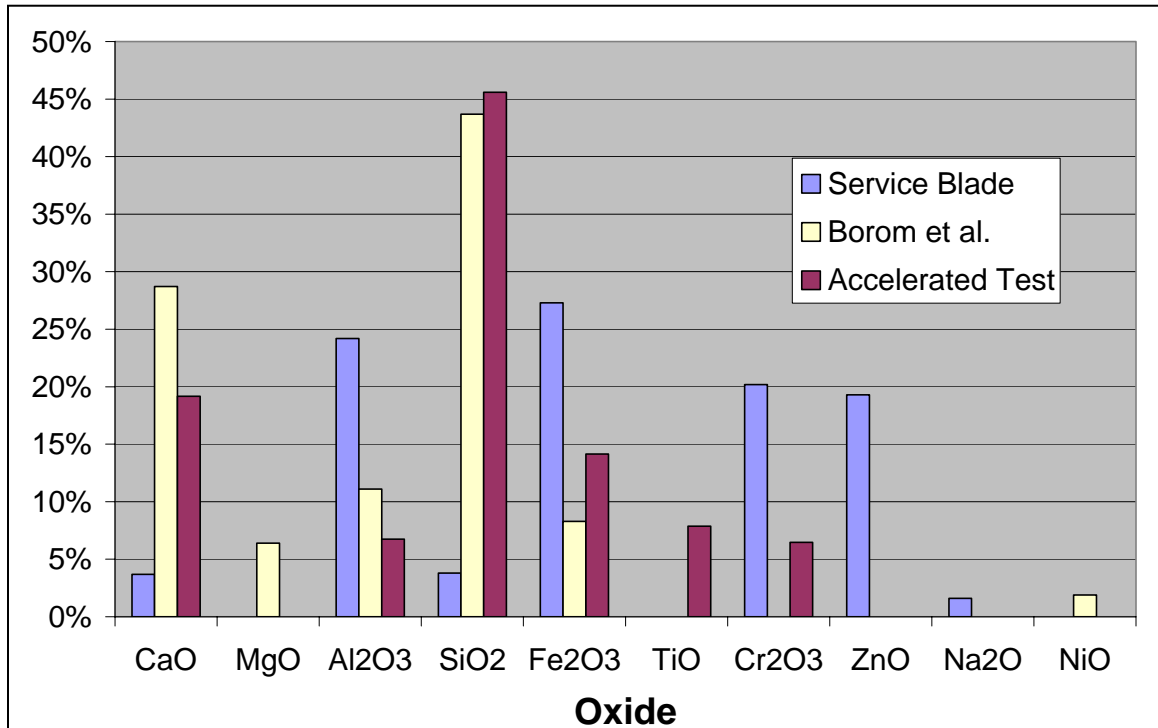


Figure 12: Graphic comparison of the essential elements in deposits on a land-based turbine blade, aircraft service blade (as reported by Borom et al, 1996), and an accelerated test sample. Percentages correspond to the % by weight.

Figure 11(b) illustrates another important point regarding turbine blade deposition. Note the area circled near the bottom left corner of the SEM scan. The different colored regions represent different chemical compositions and in this case are identified as TBC material and deposit-laden material. This area shows that even in these accelerated tests, solid-state diffusion occurs as the TBC ceramic materials mix with the ceramic compounds in ingested particulate similar to the corrosion processes that can attack TBC during prolonged operation (Krishnan et al, 2003).

It is important to note that though SiO_2 is the primary component of the earth's crust and the seed particulate (roughly 60% by weight), the mass fraction of less abundant elements such as Ca and Fe are more conspicuous within the deposit. Each of these minor elements is less than 10% as abundant as Si in the earth's crust and the seed particulate, yet each is present in quantities of 30-80% of the most abundant element (Al or Si) in the deposit for the points at which x-ray spectra were taken. This trend held true for both accelerated deposits and service turbine blades. Additionally, the turbine blade samples exhibited little constituent stratification in the deposit layer. This is similar to the results given by Borom et al. in which the chemical composition of the deposits seemed relatively homogeneous (i.e. roughly constant through the thickness) (Borom et al, 1996). From the data in Table 3 it is clear that elements such as Fe, Cr, and Ca exhibit relatively constant abundance within the deposit layer. This indicates that accelerated deposition results in a homogeneous deposit layer similar to those observed in real service hardware. Thus, all indications suggest that accelerated deposition occurs by the same processes and is hence similar to deposits formed on in-service turbine hardware.

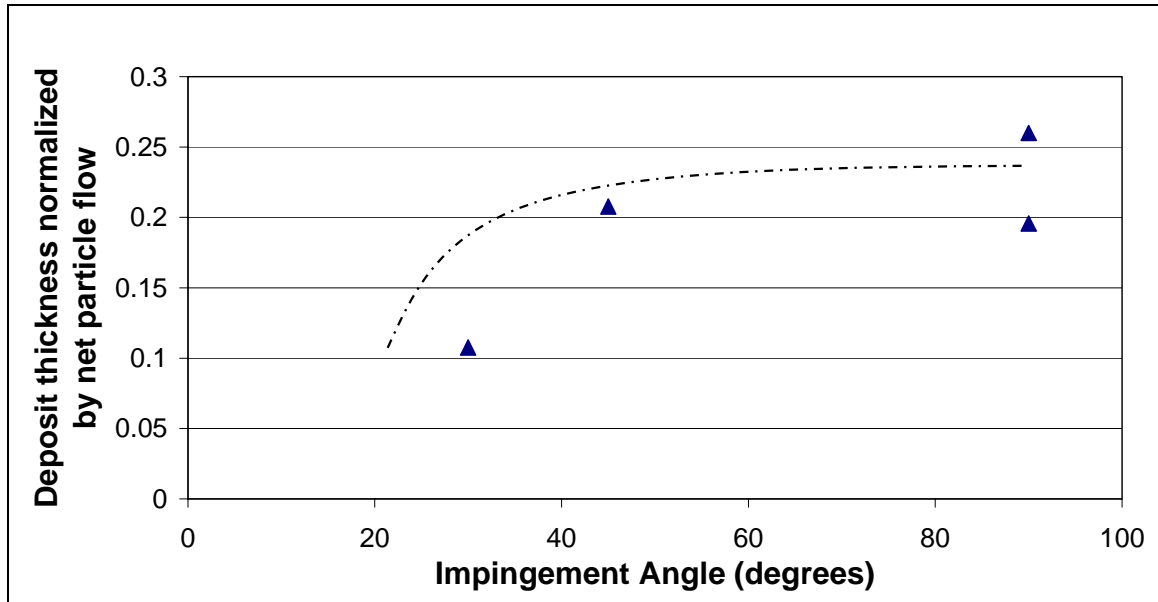


Figure 13: Normalized deposit thickness as a function of impingement angle for four accelerated tests on TBC-coated samples. (Curve for illustration only.)

Influence of Angle

A limited number of tests (four) were conducted with the same jet Mach number and temperature, but three different flow angles to determine the influence of impingement angle on deposition. The average deposit thickness measured with the Hommel surface profilometer was normalized by the net throughflow of particulate to obtain a normalized deposit thickness. This is plotted vs. impingement angles from 30° to 90° in Figure 13 (see Figure 5 for the definition of angle). Though the data are limited, there is a noticeable trend to thickening deposit with increasing angle. This corroborates well with measurements from Bons et al. which showed the leading edge zone (where flow angles approach 90°) to be the strongest candidate for deposition (Bons et al, 2001). The same study highlighted the amplified effects of material erosion in this same region of the blade, consistent with Tabakoff et al.’s finding that erosion also increases with increasing impingement angle (Tabakoff et al, 1995). Since both of these degradation mechanisms

rely on inertial impaction as the primary motive force, this finding is not altogether unexpected.

Another observation that may prove worthy of further study is that the statistical roughness factors (e.g. Ra, Rt, etc...) peaked at an impingement angle of 45° even though the deposit thickness dropped monotonically with angle. Figure 14 shows this relationship for Ra and Rt. Further investigation of this phenomenon is required to establish the order of this relationship with angle and determine its physical cause. It is possible that 45° is the angle at which the various degradation phenomena combine for a most aggressive attack on the TBC surface. Particularly deposition and erosion would tend to offset each other. It is possible that on either side of the 45° angle, one dominates the other. Above 45° from the flow path, deposition would dominate, resulting in an orderly deposition of material in homogenous layers. Below 45° , erosion would dominate, resulting in a constant smoothing of the surface by fine particles removing local peaks.

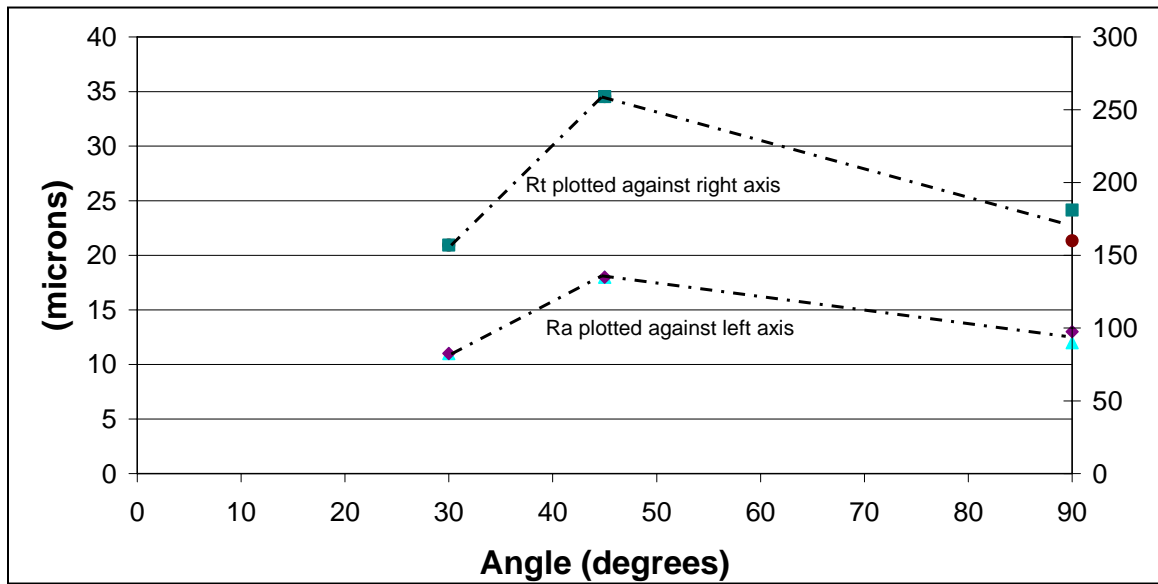


Figure 14: Roughness factors (Rt and Ra) as a function of angle to the flow path. Note that both roughness factors peak at 45° from the flow path.

Influence of Particulate Concentration

Again, only a very limited number of tests were conducted at constant Mach number, temperature, and impingement angle but with different particulate concentration (ppmw).

These results suggest a direct relationship between deposit thickness and particulate ppmw, though it is less pronounced than that with angle. By increasing particulate concentration in the air flow, the turbine simultaneously experiences an increase in erodent as well as an increase in potential deposit particulate. Thus, the erosion and deposition mechanisms may balance each other for this flow temperature and Mach number. Little change was observed in roughness statistics as a function of particulate concentration.

Influence of Temperature

Borom et al reported that turbine blade deposit accumulation did not occur in aircraft turbines with an air plasma sprayed TBC below a threshold temperature of 1090°C (Borom et al, 1996). Consistent with this finding, test runs at or above 1100°C had significant deposition and topological change to the TBC while a single run conducted below 900°C showed practically no change in topology and no detectable deposition. This temperature threshold is also dependent on other environmental and operational factors including surface condition, since some of the real turbine deposits examined during this investigation were formed at documented turbine inlet gas temperatures below 900°C.

Chapter 4: A Proposed Method for a Theoretical Estimate of the Thermal Resistance of Deposit Layers

A careful analysis of the deposits on real turbine blades and accelerated samples may yield insight into the bulk thermal conductivity of the deposit layer. As mentioned earlier, in many life models of turbine blades, the boundary conditions are converted to account for increased convective heat transfer due to an increase in surface roughness, but few models also consider the thermal resistance imposed by a finite layer of deposit with a low thermal conductivity. Such a layer would have the effect of lowering the actual temperature of the blade surface and could account for the apparent increased survivability of turbine blades above the predictions of maintenance cycle models (Soechting, 2003).

The thermal conductivity of a porous deposit can be estimated by applying equations presented by Robinson et al. for analysis of coal ash particles (Robinson et al, 2001, pt 2). Equation 6 presented here is valid for deposits with low porosity (χ_{solid} approaching unity) and was developed in discussion with Dr. Larry Baxter, a co-author in Robinson et al's study (Baxter, 2004).

$$k_{effective} = \frac{k_{solid} \chi_{solid} + k_{gas} (1 - \chi_{solid})}{\tau} \quad (6)$$

This relationship defines the effective, bulk thermal conductivity of a material based on the thermal conductivity of the physical components (both solid and gaseous) that comprise it as well as the structure of the deposit as defined by the porosity and the parameter τ known as the tortuosity. The tortuosity is a number greater than unity developed from the microstructure of the material that depresses the total thermal conductivity of the deposit by accounting for voids, contact resistance between particles, and heat flow pathways in directions other than the bulk direction. This parameter is the inverse of the structural parameter defined by Robinson et al in their analysis of coal ash deposits (Robinson et al, 2001, pt 2). Figure 15 is a schematic useful for illustrating the concept of tortuosity. Gray lines represent grain boundaries between grains (white) and voids (black). Bulk heat transfer is shown by a red arrow while the actual path taken by diffusing heat energy is depicted by the red curve. Note that though bulk motion is perpendicular to the two surfaces of a porous material, the actual heat transfer takes a much longer path through the solid portion of the material, diffusing through grains and along their edges.

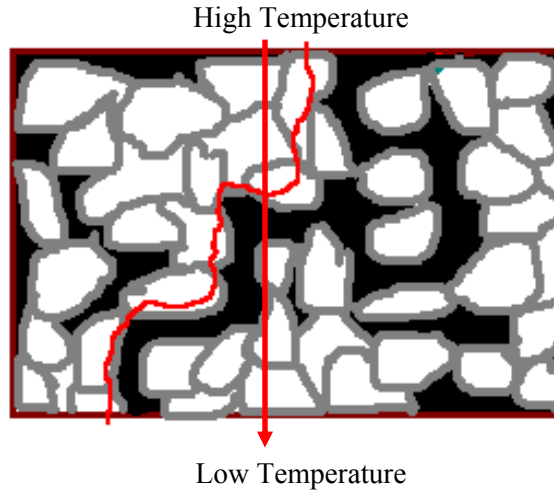


Figure 15: Schematic showing tortuosity through a porous solid material. Gray lines represent grain boundaries between grains (white) and voids (black). Bulk heat transfer shown by red arrow; actual path shown by red curve.

SEM analyses determined the bulk elemental composition of deposits to conform roughly to the data given in Table 3. By using these average elemental compositions along with the accepted thermal conductivity of the given materials, an estimate of the thermal conductivity of the solid fraction (k_{solid}) can be made. This estimate is shown in Table 4.

Table 4: Estimated bulk k_{solid} for turbine blades and accelerated samples. Thermal conductivities for constituent compounds taken from various sources.

Composition of Deposits by element										Bulk k_{solid} [W/m-K]
	CaO	MgO	Al ₂ O ₃	SiO ₂	Fe ₂ O ₃	TiO	Cr ₂ O ₃	ZnO	Na ₂ O	
service blade	3.7%	N/A	24.2%	3.8%	27.3%	N/A	20.2%	19.3%	1.6%	12.4
accelerated sample	19.2%	N/A	6.8%	45.6%	14.1%	7.9%	6.5%	N/A	N/A	7.6
Compound Thermal Conductivity [W/m-K]	7	7.5	6.55	4	11	3.28	32.94	3.5	1.7	at about 1200K

The thermal properties of the combustion gases in a turbine roughly approximate those of air at the appropriate temperature. By using the thermal conductivity of air (0.0782 W/m-

K at 1200K) as representative of the gas phase of the deposit, only the solid fraction of the deposit (χ_{solid}) and tortuosity (τ) must be defined in order to apply Equation 6.

Examination of the deposit layers photographed in the BYU SEM laboratory (Figure 17) indicate that the deposit layers in both real turbine blades as well as the accelerated samples are two dimensional in nature, consisting of relatively homogeneous layers with little three-dimensional structure such as columns and branches more common in the ash deposits of boiler scale.

Boiler scale is a three dimensional deposit consisting of branches and columns. Robinson et al. reports that the solid fraction of boiler deposits rarely exceeds 0.3 (even after sintering) due to the three-dimensional nature of the deposits. Images of these three dimensional structures both in cross-section and at the surface are shown in Figure 16 (Robinson et al., 2001, pt 2).

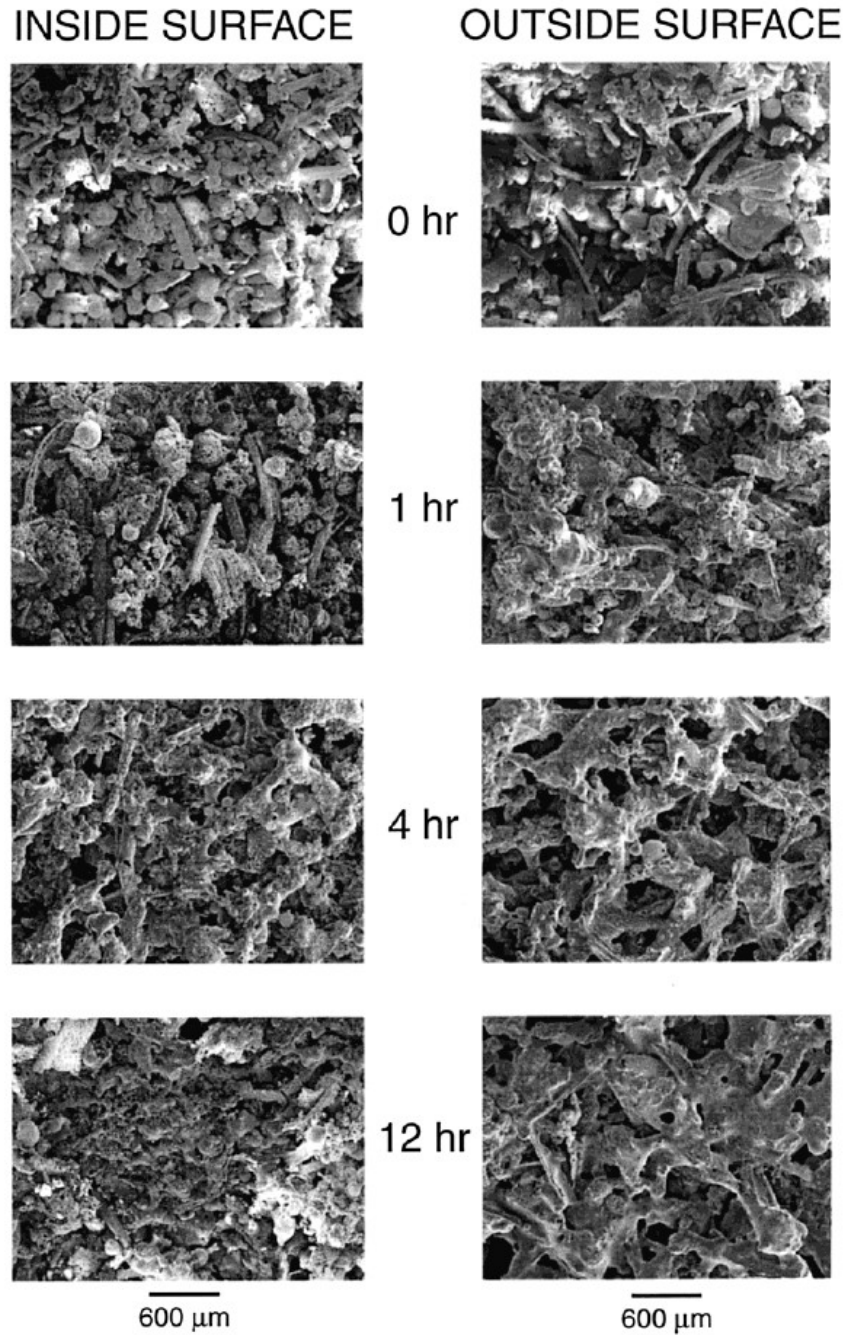


Figure 16: Electron micrographs of the inside and outside surface of deposits that have been sintered for 0, 1, 4, and 12 hours. These deposit samples were directly carbon coated and analyzed with the SEM, as described by Robinson et al. Pictures and analysis taken from Robinson et al., 2001, pt 2

Figure 17 shows a representative example of the layering typical to turbine deposits (See also Figure 10b for a similar example of layering). The dissimilarities between the boiler

deposit shown in Figure 16 and the turbine deposit shown in Figure 17 are dramatic.

Note that the turbine deposit cross-section shows relatively well-packed structures with a majority of boundaries between grains and voids lying generally parallel to the surface of the substrate. Layered deposits such as these suggest that the structure as a whole has been aggregated in a linear fashion much like stacking particles on top of each other in an ordered manner.

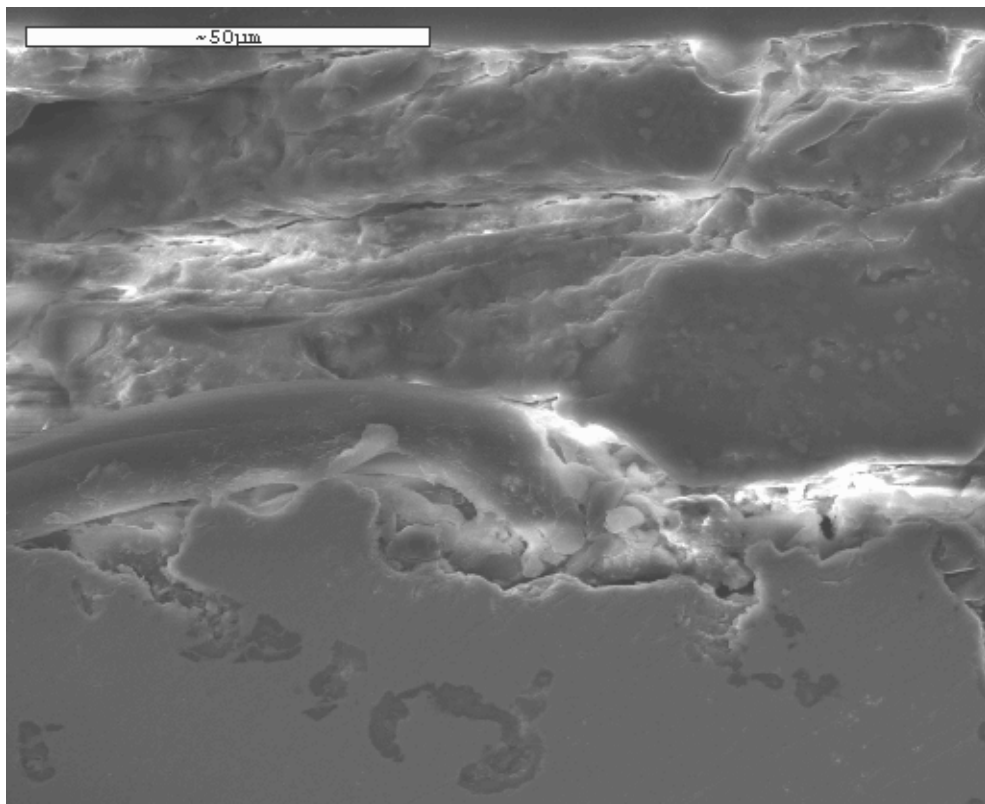
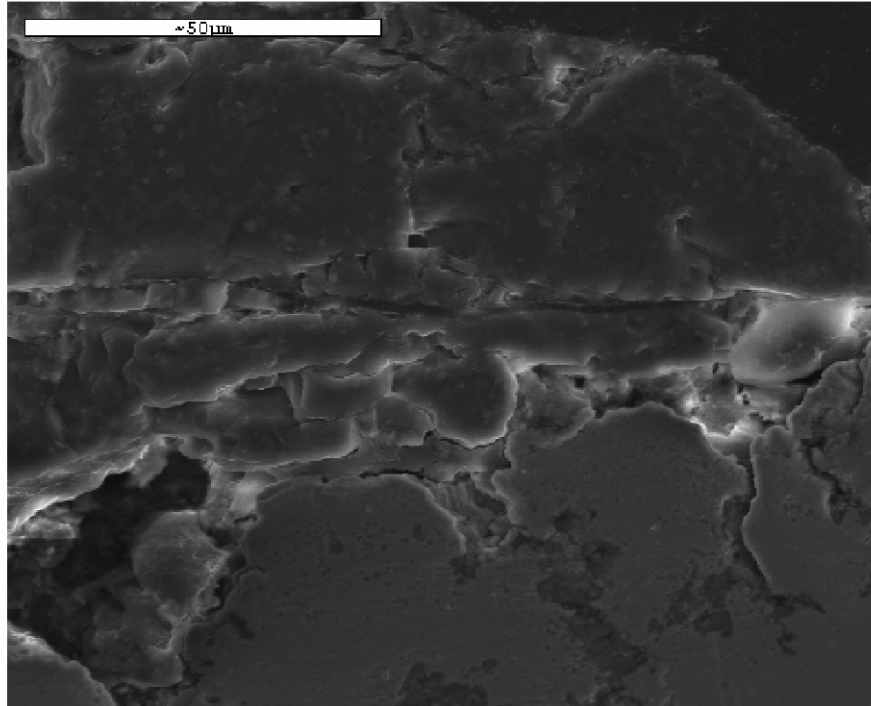


Figure 17: Cross section of accelerated deposit sample. Note layering and general absence of voids indicating two-dimensional structure.

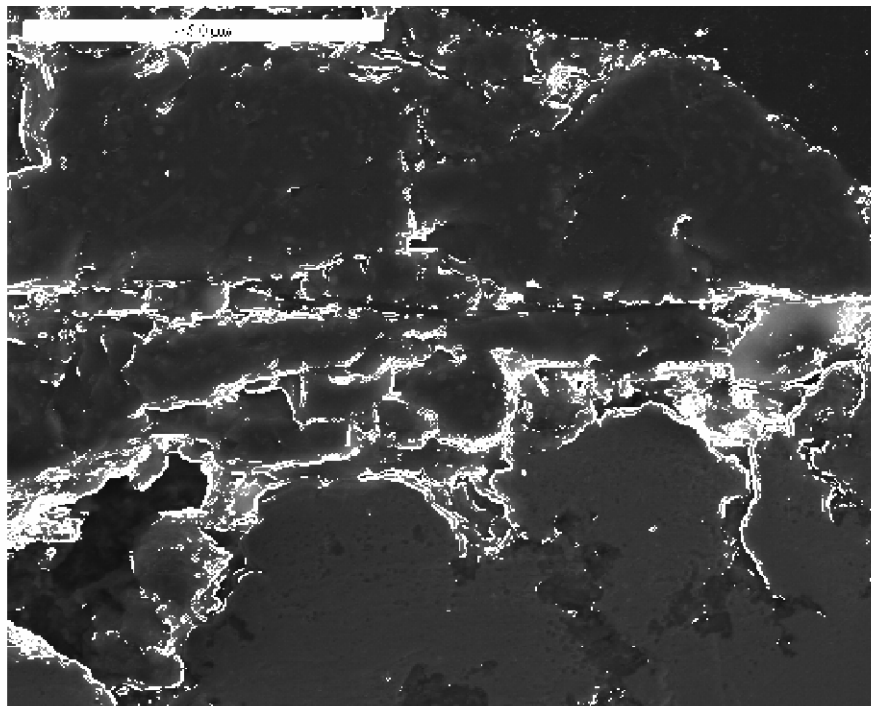
One accelerated deposit coupon was cross-sectioned into six pieces, allowing for six total surfaces to be prepared and analyzed by the SEM in two different locations each. This

series of twelve images showed similar, two dimensional layering throughout the deposit. Similarly, five separate images taken from various locations on a single service turbine blade repeatedly showed the same layering structure. (See Appendix D for a guide to the images included on the accompanying CD.) This homogeneity in structure across several locations on a single sample and across both accelerated and service deposits indicates that a cross-section image is reflective of the 3-dimensional structure of the deposit. Therefore, it follows that both the porosity and the solid fraction can be reasonably estimated from the cross-sectional pictures of the deposit layer obtained from the SEM analysis. Considering the deposit layers to be homogeneous and similar in structure throughout the entire layer, it can be assumed that the ratio of solid space to total space in any planar cross section is equivalent to the solid fraction of a volume of deposit.

It is proposed that these planar solid fractions as well as the tortuosity can be determined using image analysis tools in the MatLab software package with a succession of four analysis modules. Only preliminary work has been completed at this time, so the discussion that follows is an as yet untested roadmap. The first of the modules would reduce the SEM image to a matrix of pixel brightness values. Module I has been prepared and tested on representative SEM images; code is included in Appendix E and an illustration of the technique is shown in Figure 18. The module sequentially examines the pixel array in the 8-bit SEM image in order to locate pixel brightness gradients typical of grain boundaries and in-plane/out-of-plane boundaries using a simple differencing formula.



(a)



(b)

Figure 18: Before and after images from Module I processing. Image (a) shows an SEM picture of a deposit cross section. Image (b) shows a cross section image modified to detect image gradients denoting grain boundaries.

At each location in the array, a difference between the current array position's pixel brightness and the pixels two positions to the right and down is determined. If either difference is greater than a chosen threshold value (default to 20 on the 256 color scale), a gradient is indicated and marked by setting the intermediate pixel between the current position and the differenced position to white (pixel value 255). After the examination of the entire pixel array, the image has a series of white pixels along the edges of grains and the structures in the cut plane of the cross-section.

This image would then be passed to a second module. Module II has not yet been developed, but it is proposed that using a curve-fitting tool in Matlab, a code could be developed to divide the SEM image into small regions where second and third order curves could be fit to the white pixels along grain boundaries. These curves could be added to the image as white pixels (value 255) essentially "connecting the dots" created by Module I. These curves would create a system of boundaries throughout the image that would close the shapes suggested by the gradient detection module. These individual regions bounded by curves would correspond to grains, in-plane regions, and out-of-plane regions in the SEM cross-section. Figure 19 shows a manually-produced sample of what such an image would look like. It has been prepared by taking the image shown in Figure 18(b) and manually connecting the dots using a drawing tool. Though Module II would create a system of white boundaries, this representation has been prepared in red for clarity.

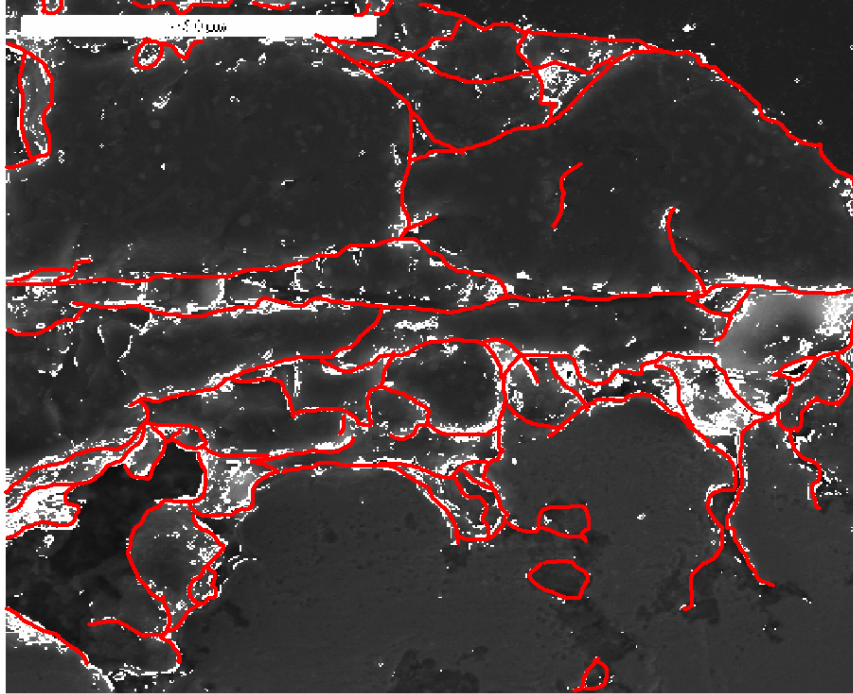


Figure 19: Sample image of what Module II would produce. Though curves would be white (8-bit image) the curves shown have been prepared in red for clarity.

Once these boundaries are established, a third module would then locate and examine the interior of each closed region. This module has not yet been developed. Once a grain area is defined, the program would attempt to establish whether the interior of the bounded region is either in-plane with the cross section or out-of-plane. In-plane areas would correspond to solid fractions while out of plane areas correspond to voids in the cut plane.

Visual analysis of the SEM pictures has indicated that the primary difference between in-plane areas and out-of-plane areas is not related to the color or absolute brightness of individual pixels within the image. Color in the SEM image corresponds roughly to chemical composition; with a fairly homogeneous deposit layer, similar colors are seen

throughout the layer regardless of distance from the cut/focus plane. Similarly, individual pixel brightness corresponds to SEM-related factors such as edge charging, intensity of the electron beam, and polishing level, making it impossible to process the image accurately by examining only the individual pixel brightness. Despite these challenges, those areas thought to be in-plane show very little variation in color or brightness from pixel to pixel within a grain/bounded area due to the polishing process used to create SEM samples. Alternately, areas out of plane show texturing and shape resulting in great variations in the relative brightness of the pixels in such areas. This is particularly true for SEM settings resulting in charging. Charging is a phenomenon that occurs when the scanning electron beam is captured on a surface, resulting in the accumulation of electrons and a net negative charge. This typically occurs on textured surfaces in an irregular fashion while flat surface remain relatively uncharged (Squire, 2004). Since flat areas are in-plane, charging would tend to accumulate on textured areas that are out of plane, resulting in a wide variation in local pixel brightness as the charging accumulates along rough edges in out-of-plane regions.

Consequently, this third module would determine in-plane areas by first locating a bounded area defined by white boundaries set by the first two modules and then comparing the brightness value of all interior pixels to each other. If the standard deviation of this group of pixels is lower than a threshold (yet to be determined), then the area may be considered in-plane, and the brightness value of all pixels should be changed to 255 corresponding to white. Otherwise, the brightness value would be changed to 0 corresponding to black to denote the area as out of plane. Figure 20 continues the

illustration of this process from Figure 19 and shows what an image might look like at the conclusion of the proposed Module III. This image has been prepared manually using image processing programs. The boundary lines in Figure 20 continue to be shown in red for clarity though the proposed processing for Module III would convert these boundaries to white. In-plane regions are white and out-of-plane regions are black.

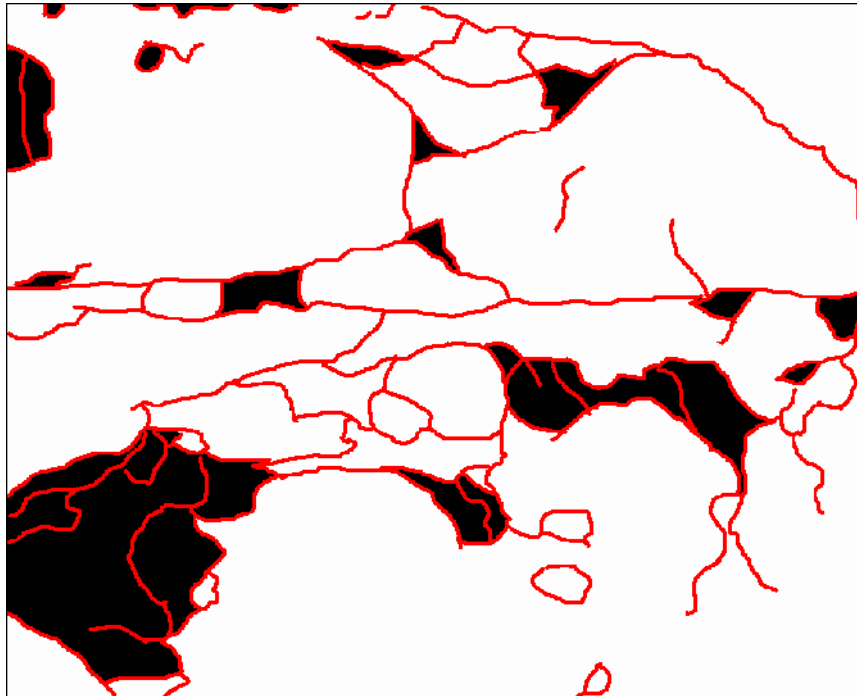


Figure 20: Sample image of what Module III would produce. Though curves would be white (8-bit image), the curves shown have been prepared in red for clarity.

A porosity estimate of the newly made image is now straightforward. At the conclusion of the proposed third module, each SEM picture has been reduced to a two-color array of pixels with white pixels corresponding to edges and in-plane areas while black pixels denote areas that are out-of-plane. By merely counting these pixels, the solid fraction of a plane can be estimated as the number of white pixels divided by the total number of

pixels in the image. Under the assumption that the deposits are two-dimensional in nature, this planar solid fraction would be equivalent to the volumetric solid fraction, χ_{solid} . For the example schematic depicted in Figure 20, $\chi_{\text{solid}} = 0.88$.

By applying the two-dimensional structure assumption to the deposit layer once again, an estimate of τ may be made by examining the deposits in cross-section and developing an average of the ratio of the perpendicular heat flow path (bulk direction) to the actual path required through solid particles:

$$\tau = \frac{L_{\text{actual}}}{L_{\text{perpendicular}}} \quad (7)$$

This parameter could be developed through the use of a fourth MatLab computer program that expands on the porosity development described above. This fourth program was still under development at the time of this work's publication and sample code is shown in Appendix E. Once the two-color images are created, they would effectively map the solid pathways in a single plane that could be followed by diffusing heat energy. The valid heat transfer pathways would correspond to white pixels while black pixels would correspond to invalid diffusion pathways. Using the definition of tortuosity, this map can be used to calculate the average non-perpendicular pathway used by heat flowing through the deposit. This could be established by means of a logic loop executed by a Matlab module.

A series of evenly spaced points along the top edge of an image are selected as starting points. If the starting point is black (corresponding to a void at the deposit interface), a null value for this start point is returned, effectively removing it from an average tortuosity calculation. If the starting point is white, the module executes a logical evaluation in a loop structure to find the shortest path to the opposite side of the deposit. This would be accomplished by proceeding down a list of progressively less direct means to move from a single pixel towards the opposing side of the deposit and incrementing the pathway taken by an appropriate amount. These logical steps along with the corresponding path addition are shown in Table 5.

Table 5: Logic steps for tortuosity determination

Logic Order	Direction	Reason	Path Addition
Step 1	Step down	Most direct to deposit end	1
Step 2	Step diagonal down right/left	Continues down, slightly longer path	$\sqrt{2}$
Step 3	Step right/left	Move laterally to look for better path	1
Step 4	Step diagonally up right/left	Move laterally to look for better path	$\sqrt{2}$
Step 5	Step up	Move to new position to restart	1

Upon moving to a new pixel, the color of the pixel can be changed to an intermediate value (120) to track the pathway. This would allow the algorithm to back track from dead-end pathways without incrementing the pathway twice in determining the final pathway length. Such “backtracking” steps would be required to carry Boolean expressions to the next loop iteration directing it to begin looking for a new path at a lower point in the logic structure so that endless loops are avoided by subsequently stepping forward into a dead end and then backtracking. If at any time the path returns to the top surface, the pathway would be discarded and a null value for path length returned

so as not to artificially inflate the tortuosity estimate. The non-null value pathway lengths would then be analyzed for mean and variance to establish the representative tortuosity for a given deposit image. With τ , k_{solid} , k_{gas} , and χ_{solid} all defined, an estimate of the bulk thermal conductivity could be made using Equation 6 listed above.

Figure 21 shows an example of what Module IV may produce. Grain boundaries are shown in red for clarity, tortuosity paths in blue, in-plane areas in white, and out-of-plane areas in black. The tortuous paths shown in blue were manually drawn onto the image using basic image processing tools. The mean tortuosity for the three pathways shown in Figure 21 is $\tau = 1.1$. The same image has been used throughout this discussion to show the evolution of an SEM image into useful data for porosity and tortuosity measurements necessary for a theoretical estimate of k . For example, using the values estimated from the manually-prepared images (Figure 20 and Figure 21), Equation 6 may be used to estimate $k_{\text{effective}} = 6.1$ as opposed to $k_{\text{solid}} = 7.6$ W/m-K.

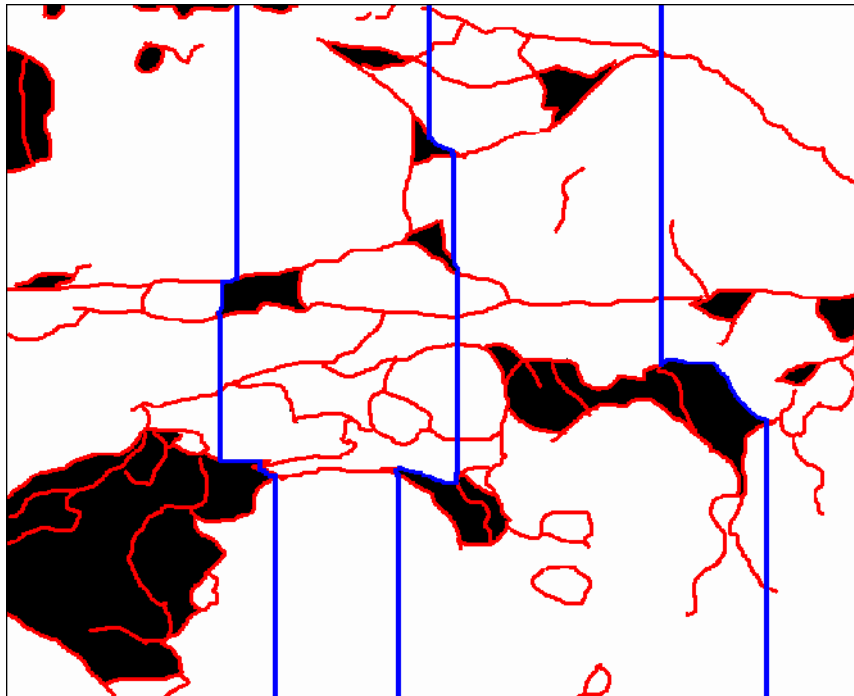


Figure 21: Sample image of what Module IV would produce. Though curves would be white (8-bit image), the curves shown have been prepared in red for clarity. Three manually-drawn sample heat transfer paths are shown in blue.

Though Figure 18 through Figure 21 show manually-produced representations of porosity and tortuosity, it is quite evident from visual inspection that over 50% of the deposit cross-section is solid (white areas and red lines in Figure 20). Figure 21 also roughly illustrates how close tortuosity estimates would be to unity. The blue lines that describe a “tortuous” path are nearly straight due to the small number and small size of out-of-plane regions (black areas). Though this manual illustration is not as rigorous an estimate as the processing procedure it illustrates, it does suggest that the deposits are mostly solid with a tortuosity close to unity.

Chapter 5: Experimental Determination of Thermal Resistance in 1-D Heat Flow

The accelerated deposition testing facility presents the unique opportunity to create samples of turbine blade deposits on one-dimensional coupons. By using circular wafers in the test facility, a sample can be created that is axi-symmetric and therefore suitable for one-dimensional heat transfer experiments. This is accomplished by insulating the sides of the wafer and then passing a large heat flux through the core of the sample in a roughly one-dimensional flow. By so doing, much can be learned regarding the real thermal properties of the deposit layer. Such an analysis requires the careful assessment of surface temperatures and heat flux of the entire sample from which a composite thermal resistance for the wafer and deposit layer can be established. By comparing this resistance value to a similar wafer without a deposit layer, an estimate can be made of the thermal resistance change due to the development of a deposit layer. This could then be compared to the theoretical value for thermal conductivity developed in a method similar to that described in Chapter 4 and subsequently used to update the thermal model of the turbine blade while in service.

Though no final theoretical model was presented in Chapter 4 for comparison, this chapter does present thermal resistance measurements of turbine samples. Thermal

resistances are reported rather than the thermal conductivity measurements for the deposit layer itself due to the confidentiality agreements made with the manufacturers of the turbine blade materials used in these investigations prohibiting investigation of the precise physical properties of the superalloy substrate and TBC. Thermal resistance measurements presented reflect the composite resistance of the wafer and the deposit layer (if any) present on the surface. Because all coupons used for the final experimental analysis were statistically identical (produced in the same lot by a single manufacturer), any statistically significant difference in the final thermal resistance is due entirely to the treatments made on the wafer during experimentation.

The Experimental Specimens

The specimens selected for the final experimental investigations were circular wafers of a turbine superalloy coated with an APS TBC. The overall wafer dimensions were 4.50mm thick by 25.4mm in diameter. The specimens were produced as experimental blanks by a GT engine manufacturing firm and donated to Brigham Young University for general studies of turbine engine degradation.

All specimens used in the experiments reported in this chapter were derived from the same production lot. Examinations of the geometry, surface topology, and mass indicate that the specimens are practically identical in every way before experimentation begins. Thus differences exhibited in the thermophysical properties of individual specimens are the result of exposure to test conditions including deposition and elevated temperature.

Experimental Apparatus

In order to establish nearly adiabatic conditions on the sides of the wafer, alumina silicate—a machinable ceramic—was used to build a jacket. The sample was placed on a shallow lip with the edges in contact with the jacket (see Figure 22). Approximately 80% of the front surface area was exposed to a uniform flat flame burner while the back surface was 100% exposed to the cooling system. A tube and shell heat exchanger using water was used to back-cool the sample during experiments. This exchanger integrated a heat flux transducer and thermocouple to measure (1) heat flux removed axially from the test sample and (2) the back temperature of the sample. Because of the low thermal conductivity of alumina silicate ($k = 1.08$ W/m-K) and the high heat flux forced through the core of the sample by the water-driven heat exchanger (on the order of $10\text{-}20$ kW/m²), the heat flow was treated as one dimensional.

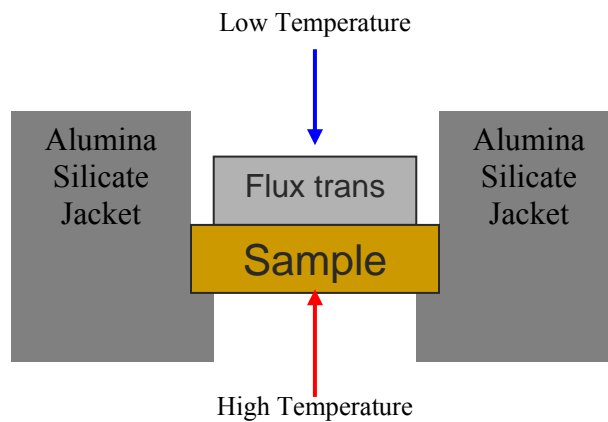


Figure 22: Schematic of testing fixture for heat flux experiments. The alumina silicate jacket on either side of the test specimen insulates it and prevents radial heat conduction. Heat applied to the front face (red arrow) and cooling applied to the back face through the heat flux transducer (blue arrow) drive the heat flux through the axis of the specimen.

The one-dimensional assumption on the heat flow allows the experiment to apply the simplified version of Fourier's Law of Heat Conduction:

$$q'' = k \frac{dT}{dx} \quad (8)$$

This equation requires some adaptation considering that the turbine blade sample with TBC and deposit layer represent a composite material. By treating the wafer as a 1-D composite wall, the composite thermal resistance relationships presented by Incropera and DeWitt may be used (Incropera et al, 2002):

$$\frac{(T_{s,1} - T_{s,2})}{q''} = \frac{1}{\left(\frac{k_{deposit}}{L_{deposit}} + \frac{k_{clean}}{L_{clean}} \right)} = \frac{L}{k_{composite}} = R_{t,cond} \quad (9)$$

Each of the parameters on the left side of Equation 9 can be measured allowing for the computation of a bulk thermal resistance ($R_{t,cond}$).

The heat flux (q'') is measured using a model HT-50 heat flux sensor manufactured by International Thermal Instrument Company. These sensors are constructed of the same material used in K-type thermocouple construction and generate a voltage linearly proportional to the net heat flux passing through the sensor in the z-direction. The sensor used has a sensitivity of 17 Btu/hr-ft² per μ Volt (46.057 W/m² per μ Volt) as reported by the manufacturer. Calibration tests confirmed this value by using an insulated bar of T-6

Aluminum with thermocouples placed at intervals along the central axis. Measurements were taken once thermal equilibrium was achieved. Information from this calibration test is shown in Figure 23. The heat flux predicted by Fourier's Law from the known thermal conductivity of T-6 Al and the temperature gradient measured on the imbedded thermocouples is plotted against the sensor reading at that point during the test. The first three points show the final stages of the transient preceding the calibration. Once the transient terminated, the heat flux predicted by Fourier's Law corresponded with the sensor to within 5% (as illustrated by the error bars in Figure 23). This heat flux sensor also incorporates a K-type thermocouple that provides a reading for the back surface temperature ($T_{s,2}$) of the sample during heat transfer experiments. The sensor was incorporated into the tube and shell heat exchanger used to cool the sample and is shown in Figure 24 and as part of the assembled exchanger in Figure 25. The heat exchanger components included galvanized steel pipe fittings, stainless steel tubing, a brass pipe-to-tubing adaptor, and RTV sealant.

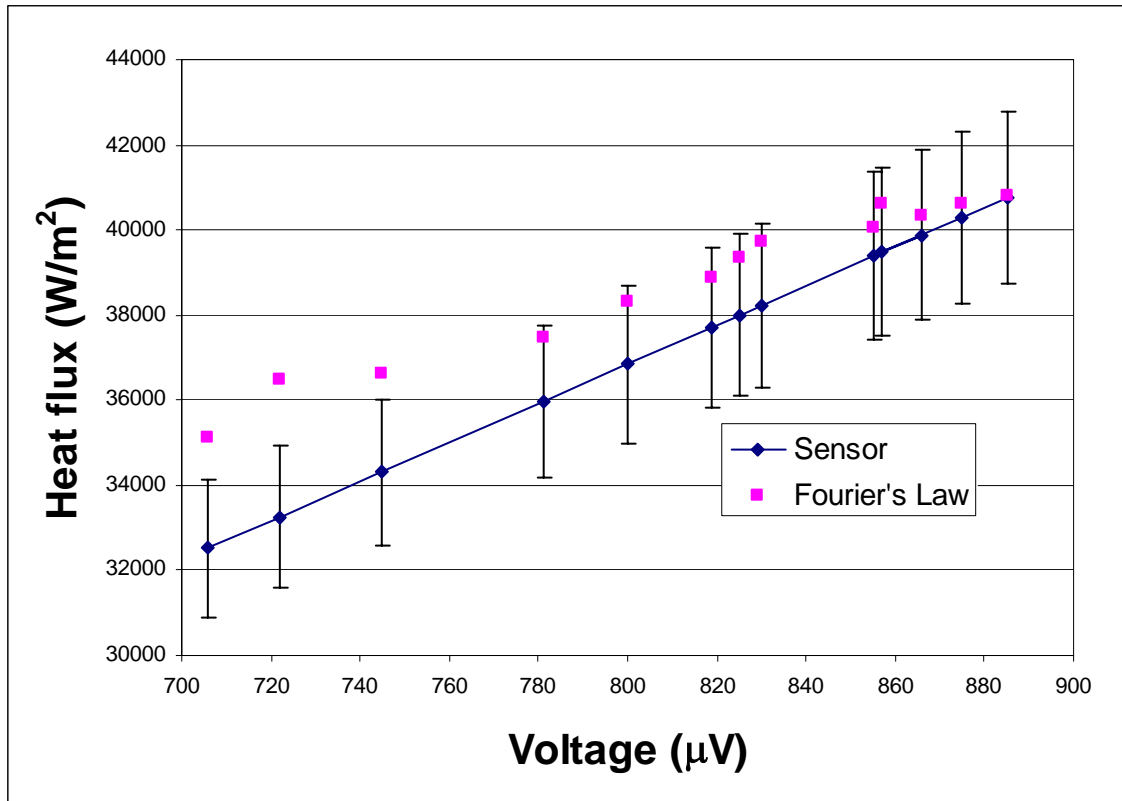


Figure 23: Calibration test data for the heat flux sensor. The sensor curve reflects the linear relationship between sensed flux and output voltage. The data points from the Fourier Law estimate of heat flux show discrete sample points during calibration testing.

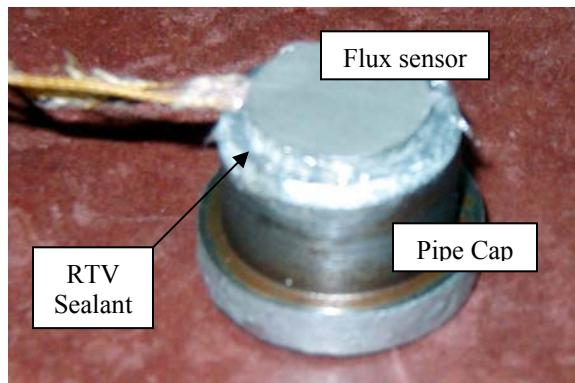


Figure 24: The heat flux sensor with imbedded K-type thermocouple attached to the tube and galvanized steel heat exchanger shell cap.

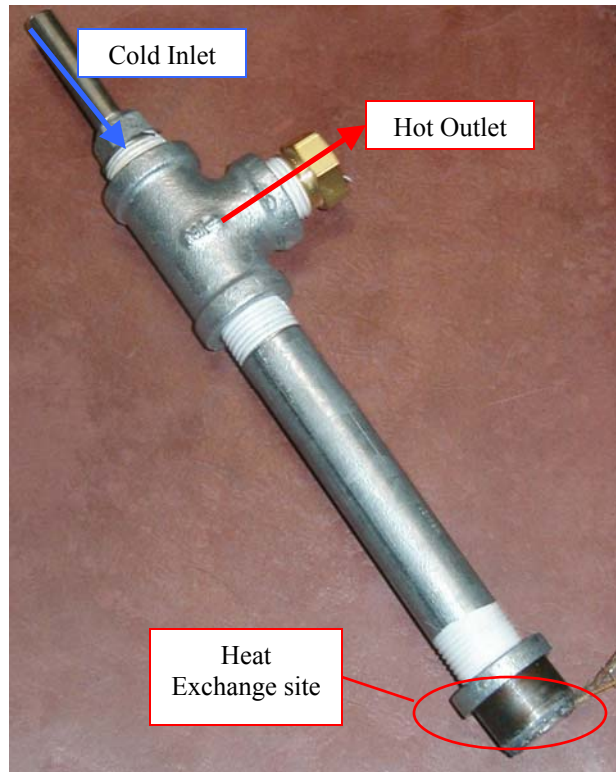


Figure 25: The tube and shell heat exchanger used in heat flux testing. The leads trailing from the cap are for the heat flux sensor and its imbedded K-type thermocouple. The exchanger was made of standard galvanized steel pipe.

The front surface temperature ($T_{s,1}$) was measured using a FLIR Systems single-color infrared (IR) camera operating with a detector and filter operating over a wavelength range of 7.5-13 μm . Initial experiments showed this measurement to be much more difficult than originally expected. Ruud et al. reported that due to the semi-transparent nature of APS TBC layers, the optical characteristics of the TBC—particularly emissivity—are extremely difficult to determine, requiring the use of complex radiant heat transfer models to quantify the radiant intensity sensed by an IR detector (Ruud et al, 1996). Consequently, a calibration of the IR camera temperature measurement was generated by thermally soaking the samples (with and without deposits) in an oven and then recording the IR camera reading. Using this technique, a calibration curve was

generated without precise knowledge of the emissivity of the samples. The samples proved to be within a single population with a 95% confidence, thus allowing the same correlation for temperature to be used in all experiments. Figure 26 shows the correlation and the confidence intervals for the IR camera calibration. Equation 7 shows the linear relationship allowing for correction of the surface temperature during testing.

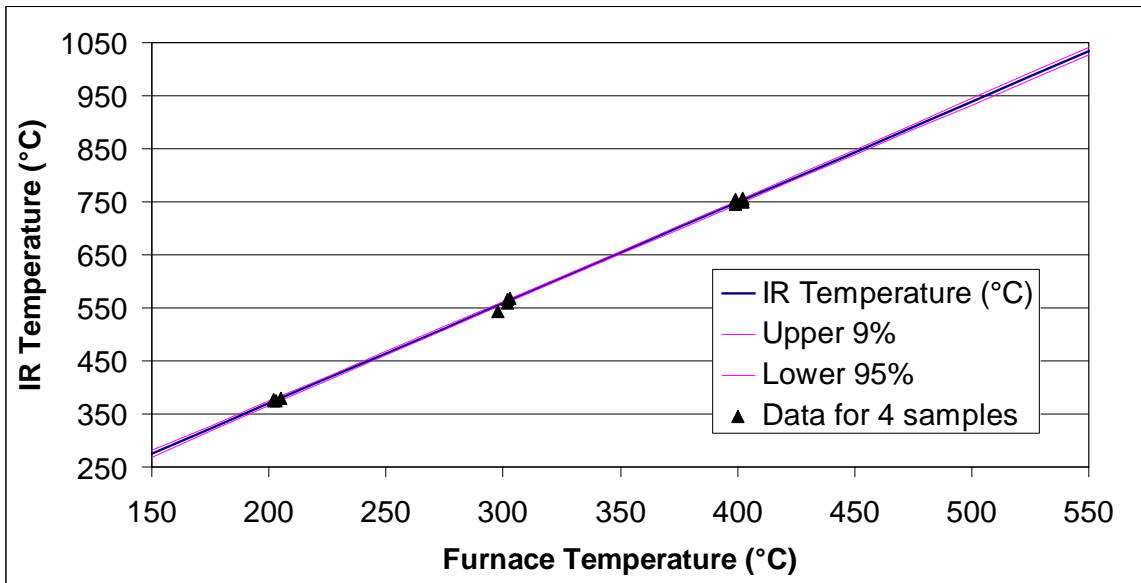


Figure 26: IR camera calibration curves. Note that the data for all samples lie along a single linear fit with extremely tight confidence intervals.

$$T_{s,1} = \frac{(T_{IR} + 9.46)}{1.90} \quad (10)$$

The apparatus used for heat flux tests is shown in Figure 27. A sample is placed in the alumina silicate jacket with a ceramic washer separating it from a steel sheet on the front face. Bolts are passed through the steel and alumina silicate jacket to a wood collar that holds a simple tube and shell heat exchanger (see Figure 25) in place against the back

face of the sample. The entire assembly is compressed together by four bolts. This assembly is then placed on a Uni-strut frame over a flat flame burner using a methane-hydrogen fuel mixture. The flat flame burner is extremely stable, producing a predictable and constant temperature condition at specific heights above the burner (Engstrom et al, 2003). The frame is angled so that the flame front does not impede optical access to the front face of the specimen. Leads from the heat flux sensor are connected to a highly sensitive voltmeter and K-type thermocouple reader. The IR camera yields temperature readings of the front face. The image is analyzed using ThermaCAM software to determine an area average of the central 50% of the sample image. This smaller area is used to insure that no thermal smearing occurs near the edges of the sample image where pixels of the sample image could mix with the signal from the steel plate image.

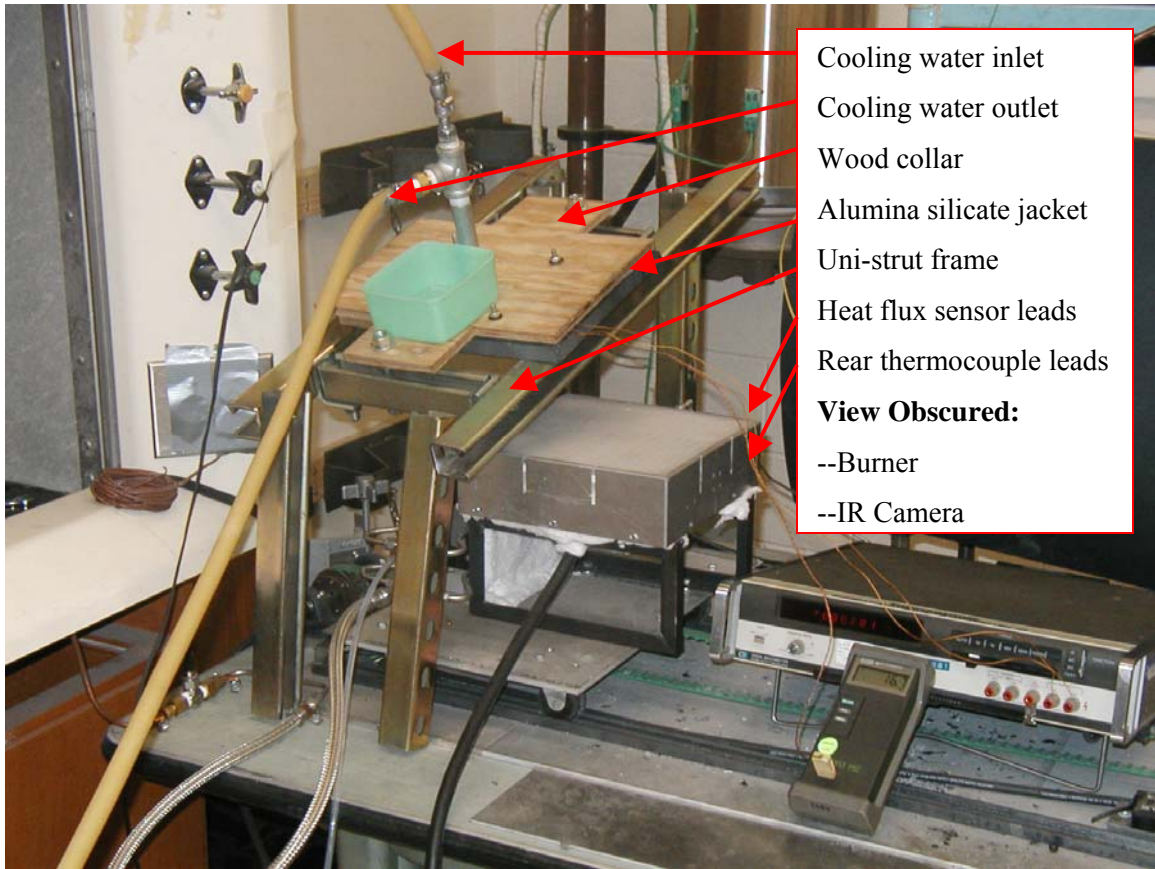


Figure 27: Heat flux test facility

Chapter 6: Thermal Resistance Measurement and Analysis

A total of 6 runs with a clean sample (no deposit) were compared to 4 runs each for three other samples: 2 samples with noticeable deposits formed at 1150°C and 1 sample with no deposits due to experimental temperatures in the test facility of 850°C. All runs were conducted over a period of two consecutive days. The data for thermal resistance for these 18 runs are shown in Table 6.

Table 6: Thermal resistance measurements for four samples. This set includes one clean (no deposits, no high temperature exposure), two samples with deposits (#6 & #7), and one intermediate sample where experimental temperatures were insufficient to evolve deposits (#9).

Sample	Runs	Mean $R_{t,cond}$ $\times 10^3$ [m ² -K/W]	$\sigma \times 10^3$ [m ² -K/W]	Signal to Noise Ratio (Mean/ σ)	Test Conditions	Max Temp [°C]
Blank	6	96.72	50.77	1.91	Flux test only	450
Coupon 6	4	50.78	34.02	1.49	Accelerated deposit	1150
Coupon 7	4	33.81	8.27	4.07	Accelerated deposit	1150
Coupon 9	4	62.01	39.33	1.58	Accelerated, no deposit	850

The data are more easily understood by examining a box plot of the various runs for each coupon as shown in Figure 28. The solid portion of each box plot shows the range of values for the 25th to 75th percentile for each data set. The “whiskers” extending from

both ends connect the inner 50% range with the maximum and minimum values in the data sets. Long boxes indicate a broad variation in the data whereas short boxes represent data sets with smaller variances. The horizontal red line in the middle of the box represents the mean for the data set. Figure 28 clearly shows that the two coupons exposed to high temperatures have a smaller variation in thermal resistance than the samples exposed to 450°C and 850°C.

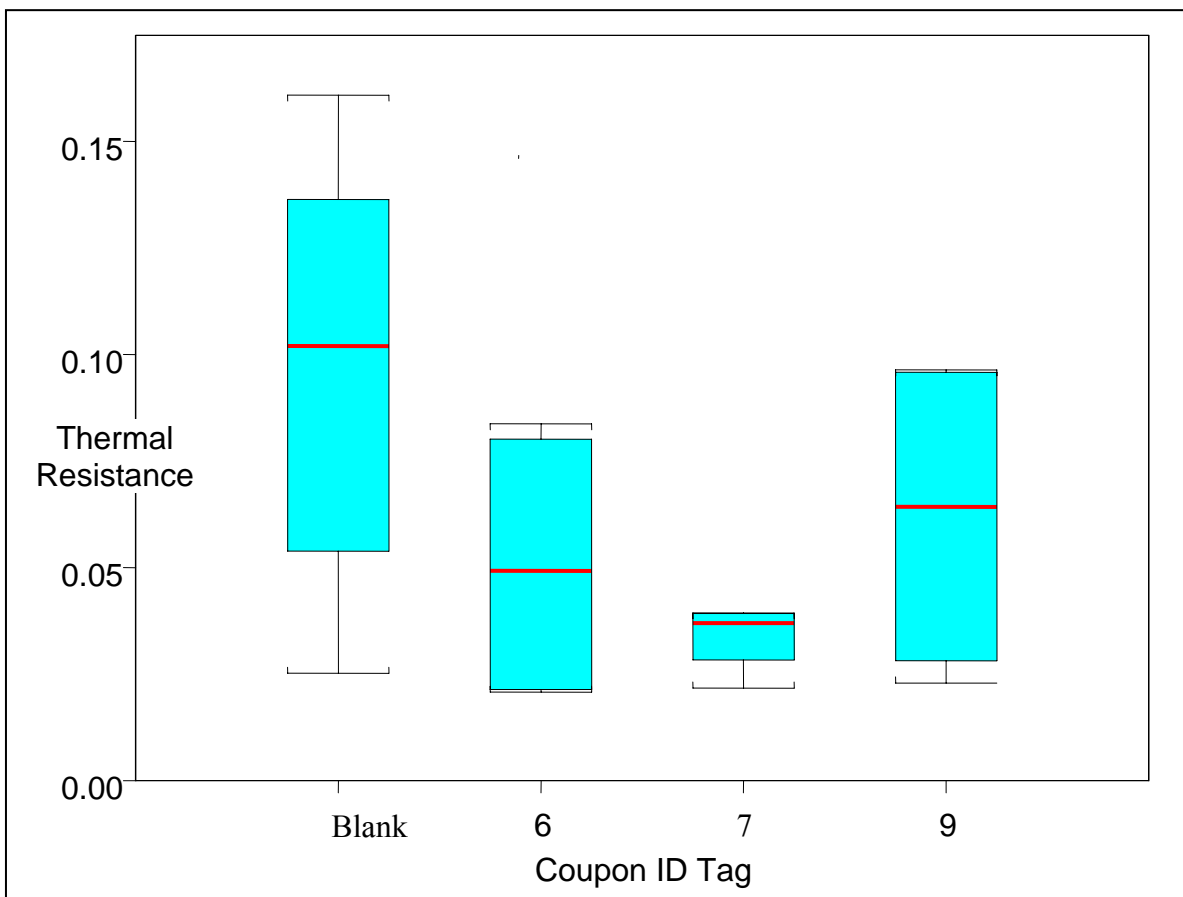


Figure 28: Box plot of thermal resistance measurements. See Table 6 for an explanation of the experimental conditions for each coupon.

The statistical analysis of the thermal resistance data sets showed coupons 6 and 7 (those with deposits) to be of a different population from the blank sample (no deposit, 450°C

maximum temperature) with a 84.6% and 95.7% confidence respectively. This high confidence level makes it likely that the deposit accumulation at high temperature has changed their thermal resistance.

The sample that was exposed to 850°C (coupon 9) showed a 72.6% confidence in being statistically different from the blank sample. This level of confidence is not reliable enough to draw a conclusion but suggests that the sample has changed structurally to a degree sufficient to be different from a blank sample. Because this sample has no evidence of deposit formation, this change would likely relate to a sintering effect in the TBC.

The clean sample shows the largest standard deviation in thermal resistances due to intermittent leaks in the cooling system during testing which seemed to plague the measurement of only this coupon's thermal conductivity. It is likely that an improvement in the testing procedure and particularly the cooling system could reduce this standard deviation. If such were possible, greater signal to noise ratios on all samples could result in a higher confidence in the statistical analysis of the difference between the various coupons.

Thermal Resistance Analysis

Figure 29 shows a diagram of the mean thermal resistance (from Table 6) organized according to the maximum temperature experienced by the coupon during testing. The clean coupon only experienced the 450°C temperature from the flat flame burner for

approximately 30 minutes while the others were subjected to combustor exit temperatures (850-1150°C) during accelerated testing for 4 hours.

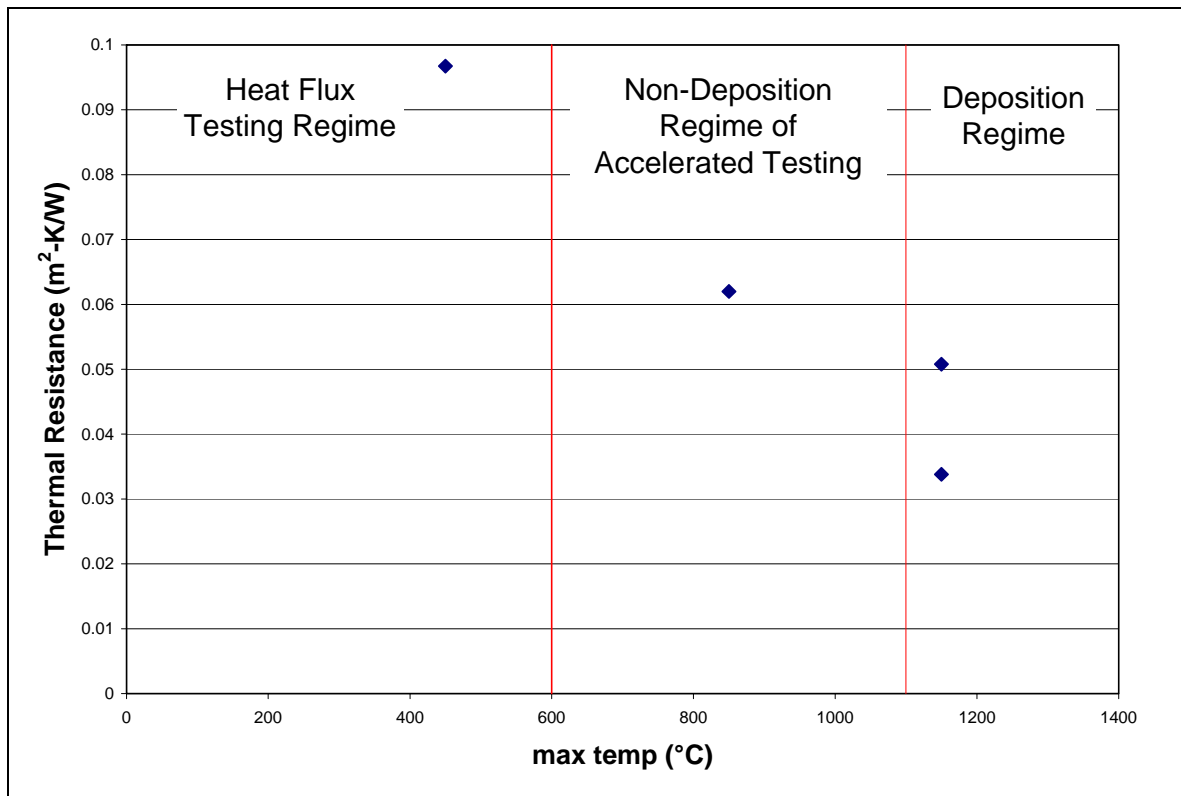


Figure 29: Plot of mean thermal resistance as a function of maximum temperature during accelerated deposition and heat flux testing. Note that samples below 1100°C do not evolve deposits. 450°C is the average surface temperature for heat flux testing and is reported as the maximum temperature only for samples that were not used in the accelerated depositional facility and therefore corresponds to blank samples.

Sintering and Deposition

Zhu et al. report that the sintering effect in TBC layers can account for a 40-57% increase in the thermal conductivity of the TBC layer (Zhu et al, 2001). Conversely, even optimistic estimates of a uniformly laid, solid deposit of ceramic oxides would likely only depress the bulk thermal conductivity of the GT engine blade by 10-15%. It is expected, therefore, that of these competing phenomena, sintering will dominate.

This expectation is borne out by the data. After exposure to 850°C test conditions, coupon thermal resistance is reduced 36%. This reduction increases to 47% and 65% for the two coupons whose maximum operating temperature was 1150°C. Despite evolving deposits, these latter two coupons showed a further decrement in thermal resistance even below the coupon that was only exposed to a lower temperature and formed no deposits.

Chapter 7: Conclusions and Recommendations

This work presents a validation of the design and operation of an accelerated testing facility for the study of foreign deposit layers typical to the operation of land-based gas turbines. This facility was designed to produce turbine deposits in a 4-hour test that would simulate 10,000 hours of turbine operation.

Conclusions

Based on the results presented herein, the following conclusions can be made:

1. The surface topography of accelerated deposits closely resembles that of actual turbine blades that have seen 10,000-25,000 hours of service.
2. The microstructure and chemical composition of accelerated deposits resemble that of actual turbine blades. The deposits are relatively homogeneous in chemical composition and appear to have low porosity.
3. A temperature threshold for accelerated deposition exists between 900°C and 1100°C for the test conditions presented herein.
4. Deposit thickness of samples developed in the accelerated testing facility generally increase as impingement angle increases to 90° (stagnation) and as particulate

concentration in the flow increases at constant flow temperature and Mach number.

The angle dependence is the stronger of these two phenomena.

5. SEM analysis suggests that both porosity and tortuosity of turbine deposits are low, suggesting that the thermal conductivity of the deposit is driven by the chemical composition of the deposit. Further analysis along the road map presented in Chapter 4 of this work would be necessary to quantify these parameters.
6. There is a statistically significant difference in the thermal resistance of clean samples that have not been exposed to high temperature and samples that have been exposed to test conditions in excess of 850°C. Further study will be necessary to separate the influence of sintering from deposition upon thermal resistance.
7. The thermal resistance of all samples decreases as maximum exposure temperature increases regardless of the presence of deposits. This indicates a strong influence on thermal resistance from sintering.

Lessons Learned

In addition to the methods, data, and conclusions presented in this work, several research avenues were pursued that did not result in valuable data. Nevertheless, these avenues are instructive in establishing some of the pitfalls inherent in the investigations related to this work. The following information can be gleaned from unsuccessful attempts to acquire the data contained in this work:

1. Air cooling and heat generation (other than combustion) are incapable of achieving a heat flux regime sufficiently great to show statistically significant differences between thermal resistances of the order expected in turbine blade deposits. It is estimated that in order to attain a detectable difference in the temperatures

- measured—and therefore be able to calculate a change in thermal resistance—a minimum heat flux of 10 kW/m^2 is needed. This heat flux was achieved in this testing using a flat flame burner and water cooling. Radiant heating, convective heating from sources other than combustion, and air cooling were all ineffective.
2. Because of the stresses inherent in thermal cycling and corrosion attacks at elevated temperatures, even exotic materials are subject to a high rate of failure. It is highly recommended that all fixturing of samples and equipment be achieved in as simple a means as possible when duplicating construction of the accelerated testing facility.
 3. Thermal expansion of nickel-based superalloys such as Inconel is quite significant at the temperatures experienced during testing. Construction means and physical restraints on the expansion of equipment should be considered carefully before operation.

Recommendations

The facility developed as a part of this research has proven an amazing success in generating deposit samples and turbine blade material samples that are comparable to service samples at a fraction of the cost and time. This invites further use of this facility to explore turbine deposits and their effects on other aspects of the heat transfer and fluid dynamics relevant to GT engines. This facility has recently been upgraded to burn with a pre-mixed fuel mixture to eliminate sooting problems and improve the efficiency of the facility. Future upgrades include a water-cooling jacket to allow for operation at higher temperatures (present operational temperature limit of 1200°C dictated by Inconel lower melting value) reflective of G-class and H-class GT engines which operate at temperatures up to 300°C hotter than this facility is presently capable of attaining.

Future Research

The accelerated testing facility described in this work is a tremendous asset in the future study of turbine degradation. Because of its ability to independently vary impact angle, temperature, particle loading, particle composition, fuel chemistry, and specimen quality, future testing with this accelerated facility could study the influence of any of these operating parameters and their effect on different turbine blade superalloys and TBC treatments. Specimens prepared in this manner could be analyzed by SEM for composition and internal structure, profilometer for surface topology, and heat flux testing for conduction characteristics. In addition, these tests can all be conducted within a period of days rather than months, greatly improving the rate at which new techniques can be tested as well as increasing the quantity of data points that can be examined for any single test condition.

Experiments to date into the thermal resistance of turbine samples resulted in some new knowledge and many new questions that will direct future research. The cumulative effects of sintering, TBC degradation, and deposit accumulation have been shown to decrease the total thermal resistance of the GT engine samples. Further testing using the accelerated testing facility could potentially separate these three phenomena into two discrete data sets for separate study.

TBC sintering can be studied by loading clean samples into an oven or the accelerated test facility. The oven would allow for sintering at well-defined ($\pm 5^\circ\text{C}$) temperatures to a

maximum of 1000°C but would not duplicate the kinetic element of flow impingement. Samples placed in the accelerated testing facility could be sintered at 800-1200°C with flow impingement but without particles being fed into the system. The temperature regimes in this facility are occasionally subject to temperature fluctuations in excess of 20°C resulting from the nuances of the air, fuel, and exhaust systems in the laboratory. Between the two facilities, however, a wide-ranging data set can be established reflecting the sole effect of sintering at various temperatures upon the TBC.

The other two effects—TBC degradation and deposit accumulation—cannot likely be easily separated from each other. Much of the TBC degradation (erosion solid-state diffusion, spallation, etc.) arises from the interaction between the particulate flow giving rise to the deposit layer and the TBC. These two mechanisms can be compared to sintering alone to determine if the sintering effect in the TBC is offset or aggravated by the combined effects of deposition and TBC degradation. Such a study can be accomplished by producing various turbine samples at varied particle loading, impingement angle, and TIT using the accelerated testing facility and then comparing them to clean samples that have undergone sintering only.

One caveat of note is that high temperature has the overall effect of vastly increasing the rate of sintering. Zhu et al. reported that TBC thermal conductivity increased as much as 40% in as little as 20 hours at 1316°C (Zhu et al., 2001). The high temperatures experienced in GT engines can result in TBC sintering occurring on the order of several hours while deposits require weeks if not months to begin forming. This time scale

dissimilarity means that the lifetime evolution of the turbine blade is dominated by the slow development of deposits after a quick burn-in phase characterized by the sintering process experienced by the TBC.

Because sintering would change the thermal resistance of the TBC very quickly, there exists considerable probability that thermal protection savings may be realized from the deposit layer. Though this work compares the thermal resistance of deposit samples to a clean, unfired turbine coupon, a more realistic estimate of the thermal resistance change in the GT heat transfer model could be made by comparing sintered but clean (no deposit) coupons to coupons bearing deposits. Further testing as outlined above would be capable of determining the savings in thermal resistance by the steady accumulation of a deposit layer following the initial depression of thermal resistance due to sintering of the TBC. This comparison may yet lead to the thermal resistance changes described in Chapter 1 of this work.

The interaction between foreign material and the TBC layer is of great interest to those studying the global heat transfer mechanism, corrosion attacks, TBC contamination by solid state diffusion, and other failures associated with extended service. The accelerated testing facility and analysis methods developed in this work invite researchers in these varied disciplines to explore the possibility that accelerated testing may be a means of generating samples for analysis of any phenomena associated with foreign material ingestion, dirty fuel burning, or extended service and offer the potential to greatly improve the understanding of the phenomena at work in GT engines.

Appendix A: Bibliography

- [1] Baxter, Larry, 2004, private communication with Jared Jensen.
- [2] Blair, M. F., 1994, "An Experimental Study of Heat Transfer in a Large-Scale Turbine Rotor Passage," *ASME J. Turbomach.*, **116**(1), pp. 1-13.
- [3] Bons, J.P., Taylor, R., McClain, S., and Rivir, R.B., "The Many Faces of Turbine Surface Roughness," *Journal of Turbomachinery*, Vol. 123, No. 4, October 2001, pp. 739-748.
- [4] Bons, J.P., 2002, "St and C_f Augmentation for Real Turbine Roughness with Elevated Freestream Turbulence," *Transactions of the ASME*, vol. 124, OCT 2002, pgs 632-644.
- [5] Borom, Marcus P., Johnson, Curtis A., and Peluso, Louis A., 1996, "Role of environmental deposits and operating surface temperature in spallation of air plasma sprayed thermal barrier coatings," *Surface and Coatings Technology* 86-87, pp116-126.
- [6] Boynton, J. L., Tabibzadeh, R., and Hudson, S. T., 1993, "Investigation of Rotor Blade Roughness Effects on Turbine Performance," *ASME J. Turbomach.*, **115**, pp. 614-620.
- [7] Brandeur, M., Schulz, A., and Wittig, S., 1996, "Mechanisms of Coke Formation in Gas Turbine Combustion Chambers," *J. Engr. Gas Turbines & Power* vol. 118, Apr 1996, pp 265-270.
- [8] Chan, K.S., Cheruvu, N.S., and Leverant, G.R., 1999, "Coating Life Prediction for Combustion Turbine Blades," *Transactions of the ASME*, vol. 121, JUL 1999, pp. 484-488.

- [9] Dunn, M. G., Padova, C., and Adams, R. E., 1987a, "Operation of Gas Turbine Engines in Dust-Laden Environments," AGARD-Advanced Technology Aero Engine Components, Paris, France.
- [10] Dunn, M.G., 2001, "Convective Heat Transfer and Aerodynamics in Axial Flow Turbines," J. of Turbomachinery vol. 123, Oct 2001 pp 637-686.
- [11] Engstrom, J.D., Butler, J.K., Smith, S.G., Baxter, L.L., Fletcher, T.H., and Weise, D.R., 2003, "Ignition Behavior of Live California Chaparral Leaves," submitted to *Combustion Science and Technology*.
- [12] Finlayson-Pitts, Barbara J., and Pitts, James N., jr. *Chemistry of the Upper and Lower Atmosphere: Theory, Experiments, and Applications*. Academic Press, San Diego: 1999.
- [13] Fintland, John, Advanced Filtration Concepts, Inc., CA, personal correspondence with Jared Jensen, 2003.
- [14] Ford, W.E., (revision), *Dana's Textbook of Mineralogy* (after E.S. Dana) 4th edn., 16th printing, John Wiley & Sons, NY 1954, p379.
- [15] Ghenaïet, A., Elder, R. L., and Tan, S. C., "Particles and Trajectories through an Axial Fan and Performance Degradation due to Sand Ingestion," ASME Paper No. 2001-GT-497.
- [16] Incropera, F.P., and DeWitt, D.P., *Fundamentals of Heat and Mass Transfer* 5th edn., John Wiley & Sons, NY 2002.
- [17] Kim, J., Dunn, M.G., and Baran, A.J. et al, 1993, "Deposition of Volcanic Materials in the Hot Sections of Two Gas Turbine Engines," J. Engr. Gas Turbines & Power vol. 115, Jul 1993, pp 641-651.
- [18] Krishnan, Vaidyanathan, Kapat, J.S., Sohn, Y.H., and Desai, V.H., 2003, "Effect of Film Cooling on Low Temperature Hot Corrosion in a Coal Fired Gas Turbine," presented at ASME Turbo Expo, Atlanta, GA, JUN 16-19, GT2003-38593.
- [19] Murray, Robert L., 1998, "Laser Doppler Anemometry Measurements in a Turbulent, Pre-mixed, Natural Gas/Air Combustor," M.S. Thesis, BYU, p17.
- [20] Rivir, Richard, 2002, private communication with Dr. Jeffrey Bons.

- [21] Robinson, A.L., Buckley, S.G., and Baxter, L.L., 2001, "Experimental Measurements of the Thermal Conductivity of Ash Deposits: Part 1. Measurement Technique," *Energy & Fuels* vol. 15, pp 66-74.
- [22] Robinson, A.L., Buckley, S.G., Yang, N., and Baxter, L.L., 2001, "Experimental Measurements of the Thermal Conductivity of Ash Deposits: Part 2. Effects of Sintering and Deposit Microstructure," *Energy & Fuels* vol. 15, pp 75-84.
- [23] Ruud, J.A., Lillquist, R.D., and Gray, D.M., 1996, "Surface Temperature Measurement of Thermal Barrier Coatings Using Infrared Pyrometry," *International Gas Turbine and Aeroengine Congress & Exhibition*, Birmingham, UK.
- [24] Seinfeld, John H., and Pandis, Spyros N. *Atmospheric Chemistry and Physics*. John Wiley & Sons, New York: 1998.
- [25] Sigal, A. and Danberg, J., 1990, "New Correlation of Roughness Density Effect on the Turbulent Boundary Layer," *AIAA Journal*, Vol. 28, No. 3, March 1990, pp. 554-556.
- [26] Smialek, J.L., Archer, F.A., and Garlick, R.G. in F.H. Froes et al. (eds.), *The Chemistry of Saudi Arabian Sand: A Deposition Problem on Helicopter Turbine Airfoils, Advances in Synthesis and Processes*, SAMPE, 3, 1992, M92-M101.
- [27] Soechting, Fred, 2003, private communication with Jared Jensen.
- [28] Squire, Sean, 2004, private communication with Jared Jensen.
- [29] Suao, Aoki, 2000, "Trend and Key Technologies for Gas Turbine Combined Cycle Power Generation in a Globally Competitive Market and Environmental Regulations," *Proceedings of the 2000 IJPG conference*.
- [30] Tabakoff, W., and Wakeman, T., 1979, "Test Facility for Material Erosion at High Temperature," *ASTM Special Publication 664*, pp. 123-135.
- [31] Tabakoff, W., Metwally, M., and Hamed, A., 1995, "High-Temperature Coatings for Protection Against Turbine Deterioration," *Transactions of the ASME*, vol. 117, JAN 1995, pgs 146-151.
- [32] Toriz, F.C., Thakker, A.B., and Gupta, S.K., J. ASME, "Thermal Barrier Coatings for Jet Engines" 88-GT-279, (1988), (presented at the Gas Turbine and Aeroengine Congress Amsterdam, The Netherlands, June 6-9, 1988).

- [33] Walsh, P.N., Quest, J.M., Tucker, R.C. jr., 1995, "Coating for the Protection of Turbine Blades From Erosion," Transactions of the ASME, vol. 117, JAN 1995, pp. 152-155.
- [34] Wenglarz, R.A., and Fox, R.G. Jr., 1990, "Physical Aspects of Deposition From Coal-Water Fuels Under Gas Turbine Conditions", Journal of Engineering for Gas Turbines and Power, Jan 1990, pp. 9-14.
- [35] Wenglarz, R. A., "An Approach for Evaluation of Gas Turbine Deposition", ASME Journal of Engineering for Gas Turbines and Power, vol. 114, April, 1992.
- [36] Wenglarz, R.A., and Wright, I.G., "Alternate Fuels for Land-Based Turbines," published in proceedings of the "Workshop on Materials and Practices to Improve Resistance to Fuel Derived Environmental Damage in Land-and Sea-Based Turbines", October 22-24, 2002, Colorado School of Mines, Golden, Colorado.
- [37] Zaita, A.V., Buley, G., Karlsons, G., 1998, "Performance Deterioration Modeling in Aircraft Gas Turbine Engines," Transactions of the ASME, vl. 120, APR 1998, pp. 344-349.
- [38] Zhu, D., and Miller, R.A., 1999, "Thermal Conductivity and Elastic Modulus Evolution of Thermal Barrier Coatings Under High Heat Flux Conditions," NASA-TM-1999-209069, NASA Glenn Research Center, Cleveland, Ohio.
- [39] Zhu, D., Bansal, N.P., Lee, K.N., and Miller, R.A., 2001, "Thermal Conductivity of Ceramic Thermal Barrier and Environmental Barrier Coating Materials," NASA-TM-2001-211122, NASA Glenn Research Center, Cleveland, Ohio.

Appendix B: Nomenclature

A_{exit}	Area at nozzle exit [m^2]
APS	Air Plasma Sprayed
d_p	Particle diameter [m]
GT	Gas Turbine
h_R	Convective heat transfer coefficient, rough surface [$\text{W}/\text{m}^2\text{-K}$]
h_S	Convective heat transfer coefficient, smooth surface [$\text{W}/\text{m}^2\text{-K}$]
HP	High Pressure
L	Deposit thickness [m]
q''_{rough}	Heat flux, rough surface [W/m^2]
q''_{smooth}	Heat flux, smooth surface [W/m^2]
k	Thermal conductivity [$\text{W}/\text{m-K}$]
M	Flow Mach number [dimensionless]
\dot{m}	Mass flow rate [kg/s]
R_{air}	Ideal gas constant for air [kJ/kg-K]
$R_{t, \text{cond}}$	Thermal resistance, conduction [$\text{m}^2\text{-K}/\text{W}$]
Ra	Centerline average roughness [μm]

R_t	Maximum peak to valley roughness [μm]
S_w/S	Total wetted surface area to planform area ratio [dimensionless]
t	time [s]
$T_{\infty,R}$	Freestream temperature, rough surface [K]
$T_{\infty,S}$	Freestream temperature, smooth surface [K]
T_1	Blade surface temperature, smooth surface [K]
T_2	Deposit surface temperature [K]
T_3	Blade surface temperature below deposit [K]
ΔT	Temperature difference from freestream to blade surface [K]
TBC	Thermal Barrier Coat
TIT	Turbine Inlet Temperature [$^{\circ}\text{C}$ or K]
v_f	Velocity of fluid [m/s]
v_p	Velocity of particle [m/s]
α_{rms}	rms deviation of surface slope angles
χ_{solid}	Solid fraction, $0 \leq \chi_{\text{solid}} \leq 1$ [dimensionless]
Λ_s	Roughness shape/density parameter (Sigal et al, 1990) [dimensionless]
γ	Specific heat ratio [dimensionless]
θ	Impingement angle [$^{\circ}$]
μ	Dynamic viscosity [$\text{N}\cdot\text{s}/\text{m}^2$]
ρ_{gas}	Gas density [kg/m^3]
ρ_p	Particle density [kg/m^3]

σ Standard deviation [as analyzed quantity]

τ Tortuosity, $\tau \geq 1$ [dimensionless]

Appendix C: Operational Procedures for Accelerated Testing Facility

The facility used for these experiments consists of grandfather equipment designed by the Department of Chemical Engineering, upgraded fuel equipment, and a completely new burner. Details of the various components that are installed parts of the Advanced Combustion Engineering Research Center (ACERC) and not unique to the accelerated deposition facility are given in this appendix.

Exhaust System

The exhaust system consists of a water-cooled exhaust jacket, three in-line automobile radiators, and an inductive fan system. The water jacket and radiators are all serviced with the same cooling water which is dumped to the drain after passing through the system. The inductive fan ensures that there is negative pressure at the inlet to the exhaust vent, causing both combustion gases and excess ambient air to be drawn through the exhaust system. This system vents to atmosphere.

Fuel System

This facility uses a natural gas fuel system drawn from standard Provo City utilities. The natural gas is primarily composed of methane though traces of other hydrocarbons and

impurities are present. Contact Questar or the BYU Physical Facilities to request an assay giving the exact chemical composition of the natural gas feed at a specific time.

The natural gas enters the system at 1-3 psi. This pressure is insufficient for the demands of the combustion facility. Therefore, the natural gas is pressurized for on-site storage at 2000 psi using a FuelMaker natural gas compressor. This compressor delivers natural gas at 3600 psi to a regulator that reduces the pressure to a level safe for storage. The natural gas is stored in four steel cylinders connected in parallel to a header pipe. This pipe then connects to a second regulator that reduces the pressure to no more than 30 psi before delivering it to the system for use in the combustor.

Storage at a pressure nearly ten times the flow pressure in the combustor ensures a uniform flow rate into the combustor throughout the total duration of an experiment. The FuelMaker compressor is also automated, replenishing the storage bottles before the header pressure drops below 1000 psi. This allows both for smooth operation during experiments and also increases safety by removing the need for a student to manually operate a compressor to replenish natural gas stocks following long tests.

For any concerns regarding the FuelMaker system, contact the installation technicians at Questar in Salt Lake City, Utah, USA. The point of contact with Questar for this facility during installation in 2003 was Dale Sevy (801-324-3652).

The fuel system incorporates a methane detector for safety. If methane is detected in the fueling area (basement) an alarm will sound and the FuelMaker compressor will

automatically shut-off. In the event of a detected leak, shut down any combustors and leave the building immediately. Contact the ACERC lab director for instructions on maintenance and emergency response.

Operation Procedures

Start-up

1. Confirm that the vertical biomass reactor is not operating.
2. Check all valves on combustor to ensure that they are closed:
 - a. Four needle valves at floor leading to tubing
 - b. Rotometer valve (finger tight only)
 - c. Ball valve on fuel board
 - d. Ball valve at wall on main line.
3. Go to the Basement to open up the main valve
 - a. Confirm that the Flare valve (unlabeled) is closed
 - b. Confirm that the regulators are properly set
 - i. Stage 1 should receive gas from the bottles at 2000-3600 psi and regulate down to 2000 psi
 - ii. Stage 2 should regulate down from 2000 psi to 20-30 psi
 - c. Open all storage bottles by turning valves completely left (counter-clockwise)
 - d. Open the ball valve on the line presently mislabeled “Methane Flare”
4. Go to the Loft to open the valves to the combustor
 - a. Open the main valve between the header pipe and the experiment isolation valve. This is the valve most upstream on the line.

- b. Turn the second (downstream) valve perpendicular to the valve body. This will send natural gas to this combustor.
5. Return to combustor to light
 - a. NOTE: THIS STEP REQUIRES TWO INDIVIDUALS TO PROPERLY AND SAFELY EXECUTE.
 - b. Ensure all four needle valves leading to the four burners are closed
 - c. Open the ball valve on the main header at the wall.
 - d. Open the second ball valve. This one is on the board downstream of the main header valve.
 - e. Slightly open main air line
 - f. Person 1: Light the butane torch and insert into the combustion chamber.
 - g. Person 2: Open a single valve leading to the combustor
 - h. Person 2: Slowly open valve on rotameter until ball reaches approximately level 10 or pilot flame ignites.
 - i. Person 1: Watch (either through view port or torch aperture) to ensure flame ignites.
 - j. Person 1: Withdraw torch and extinguish.
 - k. Person 1: Close torch aperture.
6. Monitor pilot flame for at least 5 minutes. If flame extinguishes, you have not properly opened all valves leading to the combustor. Shut off all valves on the combustor beginning with the main header valve at the wall and moving downstream. Return to Step 3 and repeat.

7. Once pilot is stable, increase rotameter setting to 20, open a second injector line, and open air line to half open.
8. Once second flame stabilizes, increase rotameter setting to 30, open third injector line, and open air line completely.
9. Once third flame stabilizes, increase rotameter setting to 40 and open fourth injector line.
10. Once fourth flame stabilizes, increase methane flow rate slowly until desired setting achieved.

Shut-down

1. Go to Loft upstairs
 - a. Shut main header valve leading to experiments. (This is the valve closest to the wall—the most upstream.)
2. Return to combustor.
 - a. Allow flame to die off. This burns all residual methane in the fuel lines.
 - b. Close header valve at the wall
 - c. Close ball valve on the board
 - d. Close the rotameter valve by turning it all the way to the right (clockwise) finger tight.
 - e. Close all four needle valves leading to the injectors
3. Go to the Loft upstairs
 - a. Close the valve that pressurizes the lines leading to experiments. This is accomplished by turning the handle parallel to the body of the valve.
4. Go downstairs to the basement.

- a. Close the ball valve on the line presently mislabeled “Methane Purge”
- b. Close the valve on all of the methane storage bottles. Turn the valve all the way to the right (clockwise).
 - i. Note: If FuelMaker compressor is operating, do not shut bottles. Wait until compressor recharges bottles and then shut
 - ii. Bottles may be left open and charging unattended if necessary.

Appendix D: CR-ROM Content Guide

Included with the printed version of this work is a CD-ROM containing several SEM images and x-ray diffraction spectra. This appendix provides a guide to the content of the CD-ROM in the hopes that further development of the theoretical models presented in Chapter 4 may be made utilizing these images.

SEM Pictures

SEM pictures of three accelerated samples and two service blades are included. Several of these include x-ray spectra showing a chemical assay of the deposit constituents. For SEM pictures that include x-ray spectra, an assay map is included in the same folder with the pictures and spectra.

1. Coupons
 - a. Coupon 5
 - b. Coupon 6 – x-ray spectra included
 - c. Coupon 8 – x-ray spectra included
2. Service Blades
 - a. SA1
 - i. SA1a – x-ray spectra included
 - ii. SA1b – x-ray spectra included
 - iii. SA1c
 - b. SA4
 - i. SA4a – x-ray spectra included
 - ii. SA4b
 - iii. SA4c – x-ray spectra included
 - iv. SA4d – x-ray spectra included
 - v. SA4e – x-ray spectra included
3. Powder x-ray – BYU SEM assay of particulate used in testing

Matlab Code

1. Module1.m – MatLab m-file code for Module I; See Chapter 4
2. Module4.m – MatLab m-file code for Module IV; See Chapter 4

Appendix E: Sample Code for Theoretical Analysis of Deposit SEM Images

This section contains code for modules I and IV for the Matlab analysis system proposed in Chapter 4 of this work. Module I detects the gradients in the image generated by an SEM and marks them with an array of white pixels. Module IV is used to process black and white images created by modules II and III to determine the tortuosity of a sample. Please note that module IV has not yet been completed, and the code presented is therefore preliminary. Matlab files for the execution of this code are included in the CD-ROM released with the printed version of this work (see Appendix D: CR-ROM Content Guide). No code is presented herein for modules II and III.

Module I: Gradient Definitions

```
clear all;
dfile=input('Enter tiff data filename without extension : ','s');
AA =IMREAD(dfile,'tiff');
[row,col]=size(AA);

meanvalue=mean(mean(AA));
fprintf('Mean intensity value is %g\n',meanvalue);

threshold = [];
threshold=input('Enter differencing threshold <20> : ');
if isempty(threshold)
    threshold=20;
end

AAfilt=AA;

for i=1:(row-2)
    for j=1:(col-2)
        diff=abs(double(AA(i,j))-double(AA(i+2,j)));
        if diff > threshold
            AAfilt(i+1,j) = 255;
        end
        diff=abs(double(AA(i,j))-double(AA(i,j+2)));
        if diff > threshold
            AAfilt(i,j+1) = 255;
        end
    end
end

figure(1);
```

```
IMShow (AA);  
title('Raw Image');
```

```
figure(2);  
IMShow(AAfilt);  
title('Gradient-Detected Image');
```

Module IV: Tortuosity

```
clear all;
dfile=input('Enter black and white tiff data filename without extension : ','s');
AA =IMREAD(dfile,'tiff');
[row,col]=size(AA);

fprintf('The deposit image width is: %g\n',col);
fprintf('The deposit image depth is: %g\n',row);

Pathnum = [];
Pathnum=input('Enter number of paths to compute tortuosity <25> : ');
if isempty(Pathnum)
    Pathnum=25;
end

AAfilt=AA;

MaxC=double(col)
MaxR=double(row)

Spacing = MaxC/Pathnum;
Place = round(Spacing/2);

for k=1:Pathnum
    Path(k,2)=[];
end

for k=1:Pathnum
    Path(k,1)=round(Place);
    Path(k,2)=0;

    %Do the path computation logic loop here
    i=2; %start in second row to avoid logic errors looking away from this pixel
    j=Path(k,1); %starting column is location for this path
    ThisPixel = AAfilt(i,j);
    last_i=1;
    last_j=j;
    last_step=0;

    while i>1 and i<row and double(ThisPixel)<>0 %start and end one pixel in from edge
        AAfilt(i,j)=120; %Mark path by changing to gray
        %look for white (255)
        %Store the path distance in Path(k,2)
        %Location of the pixel of present interest is AAfilt(i,j)
        if AAfilt(i+1,j)=255 %look down
            last_i=i;
```

```

    last_j=j;
    i=i+1;
    Path(k,2)=Path(k,w)+1;
    last_step=1;
elseif AAfilt(i+1,j+1)=255 %look down right
    last_i=i;
    last_j=j;
    i=i+1;
    j=j+1;
    Path(k,2)=Path(k,2)+sqrt(2);
    last_step=sqrt(2);
elseif AAfilt(i+1,j-1)=255 %look down left
    last_i=i;
    last_j=j;
    i=i+1;
    j=j-1;
    Path(k,2)=Path(k,2)+sqrt(2);
    last_step=sqrt(2);
elseif AAfilt(i,j+1)=255 %look right
    last_i=i;
    last_j=j;
    j=j+1;
    Path(k,2)=Path(k,2)+1;
    last_step=1;
elseif AAfilt(i,j-1)=255 %look left
    last_i=i;
    last_j=j;
    j=j-1;
    Path(k,2)=Path(k,2)+1;
    last_step=1;
elseif AAfilt(i-1,j+1)=255 %look up right
    last_i=i;
    last_j=j;
    i=i-1;
    j=j+1;
    Path(k,2)=Path(k,2)+sqrt(2);
    last_step=sqrt(2);
elseif AAfilt(i-1,j-1)=255 %look up left
    last_i=i;
    last_j=j;
    i=i-1;
    j=j-1;
    Path(k,2)=Path(k,2)+sqrt(2);
    last_step=sqrt(2);
elseif AAfilt(i-1,j)=255 %look up
    last_i=i;

```

```

        last_j=j;
        i=i-1;
        Path(k,2)=Path(k,2)+1;
        last_step=1;
    else %undo step and go back to gray position
        i=last_i;
        j=last_j;
        Path(k,2)=Path(k,2)-last_step;
    end

    ThisPixel=AAfilt(i,j); %kicks out of while when "step back" happens twice and
    accidentally lands in black

    end

    for k=1:Pathnum
        if Path(k,2)<2
            Path(k,2)=[];
        else Path(k,2)=Path(k,2)+2 %add the first row and last row pixels
        end
    end

    end

    Place= Place+Spacing;
    if Place > MaxC
        Place = MaxC-1;
    end
end

figure(1);
IMShow (AA);
title('B/W Image');

figure(2);
IMShow(AAfilt);
title('Path Image');

Mean=0;

for k=1:Pathnum
    Mean = Mean +Path(k,2);
    fprintf('Path number %g\n',k, 'is %g\n',Pathnum(k,2),' pixels long. (0 denotes Null
    Path.)');
end

```

```
Mean=Mean/(Pathnum-NullPathCount);  
fprintf('The mean path length is %g\n',Mean, 'pixels.');
```

Tort=Mean/row;

```
fprintf('The mean tortuosity of this deposit is: %g\n',Tort);
```